

## Process electrification by magnetic heating of catalyst<sup>☆</sup>

Jakov-Stjepan Pavelić <sup>a,b</sup>, Sašo Gyergyek <sup>c</sup>, Blaž Likozar <sup>a,b,\*</sup>, Miha Grilc <sup>a,\*</sup>

<sup>a</sup> Department of Catalysis and Chemical Reaction Engineering, National Institute of Chemistry, Hajdrihova 19, 1000 Ljubljana, Slovenia

<sup>b</sup> Faculty of Chemistry and Chemical Technology, University Ljubljana, Večna pot 113, 1000 Ljubljana, Slovenia

<sup>c</sup> Department for Materials Synthesis, Jožef Stefan Institute, Jamova 39, 1000 Ljubljana, Slovenia

### ARTICLE INFO

**Keywords:**  
Process Electrification  
Magnetic heating  
Catalysis  
Heat transfer

### ABSTRACT

Electrification of the chemical and energy sector is a crucial step in the transition towards a carbon neutral society. Electrocatalysis is one way to selectively steer a reaction towards the desired products which relies on the electric field effects instead of temperature, but there is another way to solely heat the reaction site. Magnetic or induction heating of magnetic nanoparticles embedded within the catalyst can selectively heat the catalyst at the reaction site. Furthermore, such rapid and selective heating enables a construction of decentralised, intermediate-scale, adaptable, containerised and responsive units, capable of flexible operation as per the European Union's new industrial paradigm. The possibility to utilize intermittent renewable energy and to operate reactors in highly dynamically responsive manner leads to energy efficiency, safer operation, reduced energy costs in downstream processing, keeping bulk fluid cold(er) compared to the catalyst grain to mention a few advantages. Recently, this concept has been successfully applied and reported but only in a relatively limited number of studies, which are reported and thoroughly reviewed in this work. This review aims to highlight and critically evaluate recent developments of magnetic materials used in magnetically heated catalysis and represent their magnetic and chemical properties in combination with an overview of reported chemical conversions. It can serve as guide to select optimal magnetic material for a targeted chemical conversion, highlighting (also schematically) their potential and restriction of use.

### 1. Introduction

Induction heating is the technology that enables contactless heating of the conductive materials. It is commonly used in domestic as well as in industrial and medical applications [1]. Closely related magnetic heating (MH) applies radiofrequency alternating magnetic field (AMF) to magnetic nanoparticles to generate heat within them. Magnetic nanoparticles are small enough (approx. up to 100 nm in diameter) that the predominate heating mechanism is relaxation (Brownian or Néel) or hysteresis loss [2]. Gao *et al.* [3] show the magnetometry measurements on various nanocrystallite sizes of Ni-Zn ferrite. The magnetization increases with the increase of nanocrystallite size from 12 to 27 nm. A sample with nanocrystallite size of 21 nm showed maximum coercivity. Therefore, it can be stated that mixed metal oxides show the highest heat recovery in the nanocrystallite size range of about 20 – 30 nm [3]. Typically, magnetic nanoparticles or nanocomposites composed of magnetic nanoparticles are contained within a non-magnetic and non-conductive vessel inserted within a coil connected to an alternating

current generator [4]. Small magnetic nanoparticles that are smaller than their superparamagnetic limit heat due to Neel's relaxation if the nanoparticles are fixed *i.e.*, immobilized and therefore not being able to rotate. Suspended magnetic nanoparticles can heat under AMF due to Brownian relaxation [5]. Fixed magnetic nanoparticles that are larger than their superparamagnetic limit (larger than approx. 16 nm for the magnetic iron oxide maghemite) and exhibit ferrimagnetic or ferromagnetic properties heat under AMF due to hysteresis losses [6–8]. At this point it should be noted that the mentioned separation of the mechanisms responsible for heating is artificial, but the distinction is very persistent in experimental-based articles. For the purposes of clarity of this review, the term induction heating will be used when heating is clearly consequence of eddy currents induced by AMF and magnetic heating when hysteresis losses are cause of heating and not differentiating relaxation mechanism. A simple representation of static and dynamic hysteresis of single domain magnetic nanoparticles is presented in Fig. 1. It should be noted that the magnetic field strength is often presented using different measurement units, such as oersted (Oe), (mili)

<sup>☆</sup> This article is part of a special issue entitled: 'Guy Marin SI' published in Chemical Engineering Journal.

\* Corresponding authors.

E-mail addresses: [blaz.likozar@ki.si](mailto:blaz.likozar@ki.si) (B. Likozar), [miha.grilc@ki.si](mailto:miha.grilc@ki.si) (M. Grilc).

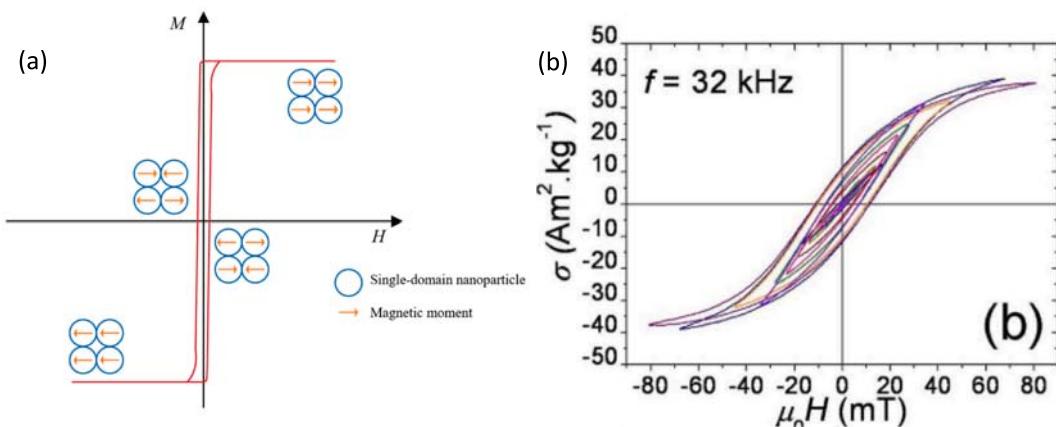


**Fig. 1.** (a) A scheme of the hysteresis loop and its correlation to the magnetic moment (own work) and (b) dynamic hysteresis loops of iron oxide magnetic nanoparticles as a function of AMF amplitudes at constant frequency. Reprinted with permission from reference [10], copyright AIP publishing.

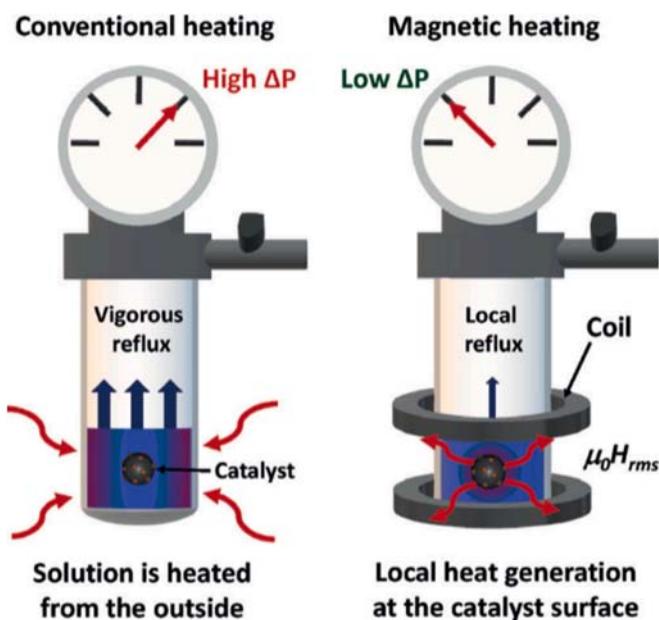


**Fig. 2.** Schematic presentation of IH and conventional heating effects on the pressure inside of the reactor system. Reprinted with permission from reference [11], Copyright John Wiley and sons).

tesla (mT), or amperes per meter ( $\text{A m}^{-1}$ ). The SI unit for magnetic field strength  $H$  is  $\text{A m}^{-1}$ , while in cgs unit system the unit is Oe. A convenient SI representation is  $\mu_0 H$ , usually in mT. Strictly speaking, this is the  $B$  field, which in air and vacuum has the same direction as  $H$  field, while its strength is  $\mu_0 H$ . Such representation is only valid for external fields while inside the material  $B$  and  $H$  fields differ in direction and magnitude due to magnetization. These units, when considering external fields, are easily converted from one to another using simple conversion factors. For instance, 1 Oe equals to  $10^3/(4\pi) \text{ A m}^{-1}$ , and 0.1 mT. Curious reader is encouraged to read literature dealing with the subject in a more comprehensive manner such as for example the work by Deatsch and Evans from 2014 [9].

Since many catalytic reactions are endothermic, the problem that is created by heating the system is a great rise of pressure inside of the reactor. One of the possible ways to minimize this problem is by magnetic heating of the catalyst bed within the reactor where the reaction mixture is heated from the inside of a reactor.

The heat is delivered from magnetic particles in direct contact with the catalyst. Then, the catalyst heats up only a small volume of the

reaction mixture which is in close contact with the catalyst while the rest of the medium is at significantly lower temperature, which causes less evaporation and a smaller pressure increase as shown in Fig. 2 [11,12]. Inductively or magnetically heated systems applied to chemical conversions are lately the hot topic in catalysis and energetics. Since the observations have been made that various particles can be inductively heated, the idea was born to try to utilize this property and use it in catalysis, which is widely present in the vast majority of chemical processes.

Implementation of the inductively or magnetically heated technology to chemical reactors could potentially replace the need to heat up the whole reactor and focus directly on heating of the catalytic particles. This way, the mass of the reactant mixture would remain near the room temperature, and the layer of the reactants adjacent to the catalyst would be heated up *via* convection through the surface of the heated particles (Fig. 3). It is necessary to note that the temperature profile shown in Fig. 3 does not contain absolute temperature, but serves merely as a graphical scheme to show that the liquid temperature in magnetically heated systems is significantly lower than the temperature on the catalyst's surface, which is where the reaction takes place. On the other hand, each of the elements in a cross-section of a reactor in a conventionally heated system exhibits significantly different temperature than that of the element in its near vicinity. It was also observed that magnetic induction can be a trigger to enhance the catalytic activity of the given material and, in turn, increase the reaction rate [13–17]. It is worth noting that inductively heated reactor systems are more robust considering the reaction parameters in comparison to the conventionally heated systems [18]. The choice of the reactor material for magnetic heating is crucial, since it needs to be made of a radio-frequency transparent material which does not heat due to induction. Most popular choices include glass, quartz and polymers such as poly(ether ether) ketone (PEEK). It is also possible, at least in principle, to employ ceramic reactors for high temperature reactions. However, for all of the materials, the highest pressure that can be applied is limited to significantly lower value than for conventional reactors made, for example, of stainless steel [2]. In short, the main advantage of inductively heated systems is their adaptability to the needs of various chemical processes, which implies the reversibility, rapidity and robustness of the system, which is also known as the  $R^3$  rule [17].

In order to have a working system, which can be efficiently heated *via* magnetic heating, catalytic activity and the heating capacities of the chosen materials has to be studied. An important value that helps quantify the heating efficiency of the material is the specific absorption rate (SAR). SAR is the rate of thermal energy generated by magnetic material under AMF absorbed by the medium and is usually determined calorimetrically. SAR is usually referred to as a figure-of-merit for

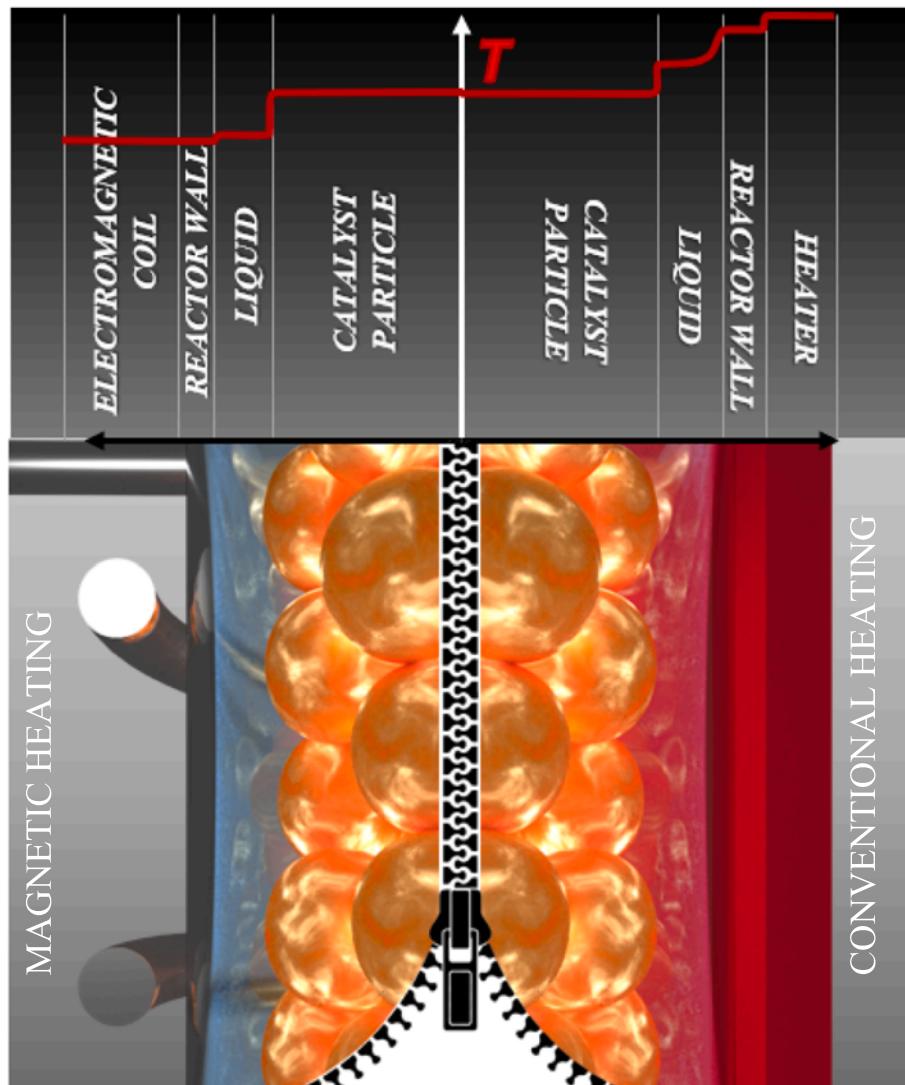


**Fig. 3.** Temperature gradient comparison between the magnetically and conventionally heated reactor system (own work).

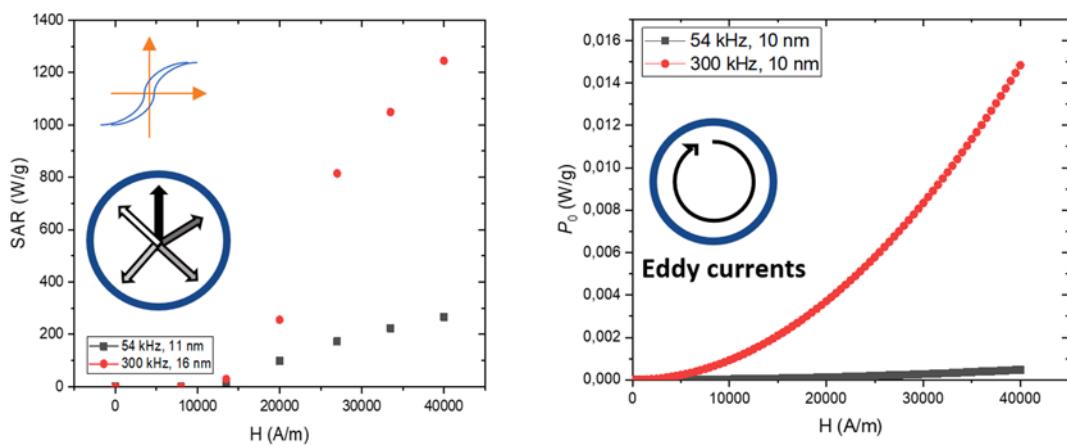


**Fig. 4.** SAR vs H dependency of iron nanoparticles, described with hysteresis heating (left) and magnetic moment direction change in a particle contribution of induction, eddy force heating to the total SAR values, described with the oscillation of eddy currents (right) (own work).

thermal power generated by unit mass of magnetic material under AMF. It is important to note that some authors refer to SAR as SLP (specific loss power) [19–21]. Another important value is the Curie temperature,

which represents the temperature point above which a material loses its permanent magnetic properties and consequently seizes magnetic heating [22].

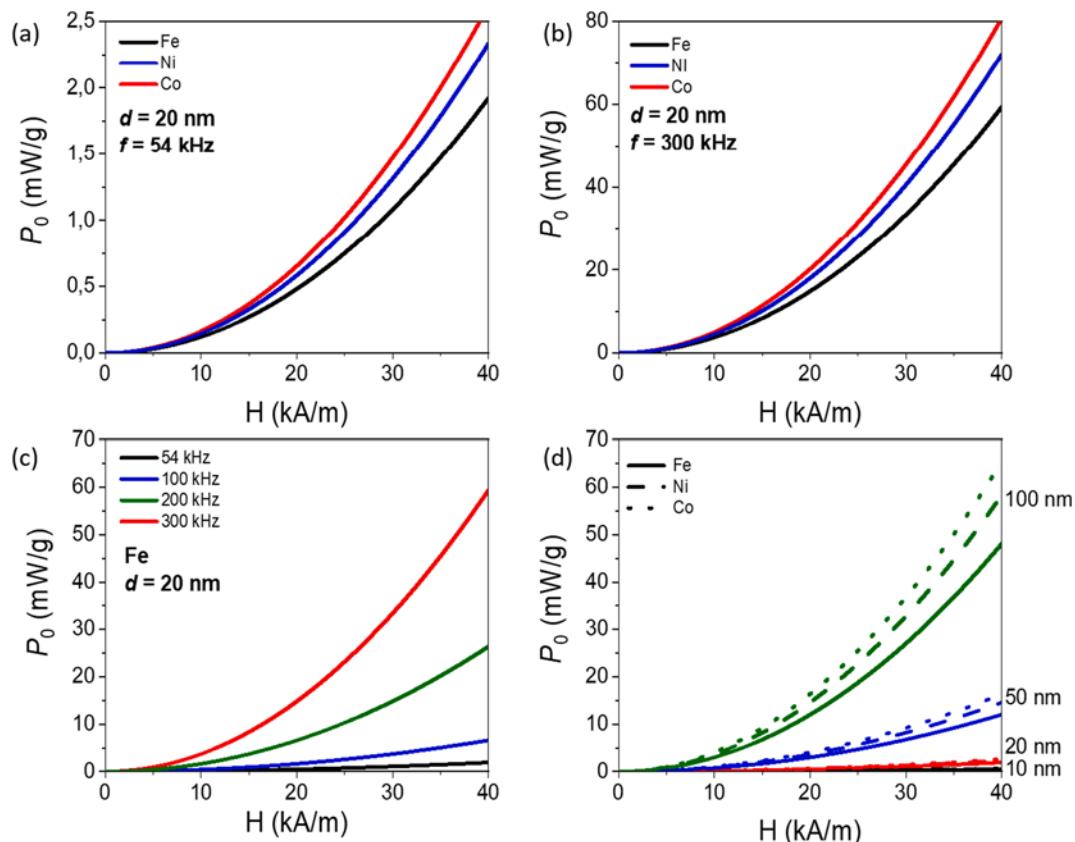


**Fig. 5.** (a) comparison of the eddy current contribution to the overall magnetic heating effect for 20 nm Fe, Co and Ni nanoparticles using AMF frequency of 54 kHz and (b) 300 kHz (c) contribution of eddy current to the magnetic heating of 20 nm Fe nanoparticles at different AMF frequencies and (d) the nanoparticle size dependency on the eddy current contribution for iron, nickel and cobalt (own work).

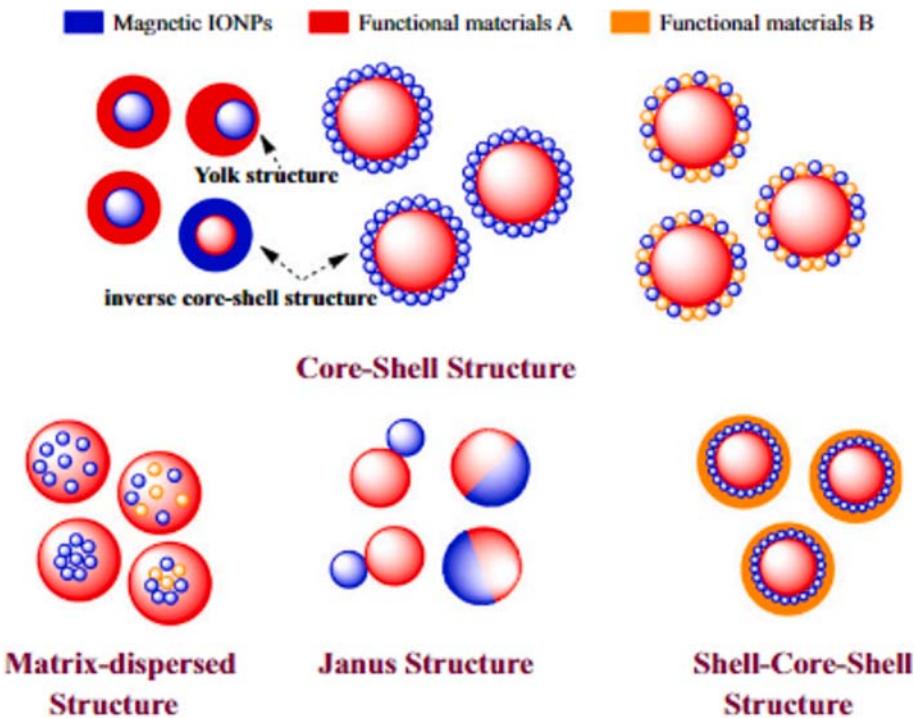


**Fig. 6.** Schematic view of the magnetic nanocomposite types, where blue-colored shapes represent magnetic nanoparticles. Reprinted with permission from reference [30], Copyright 2015 National Institute for Materials Science.

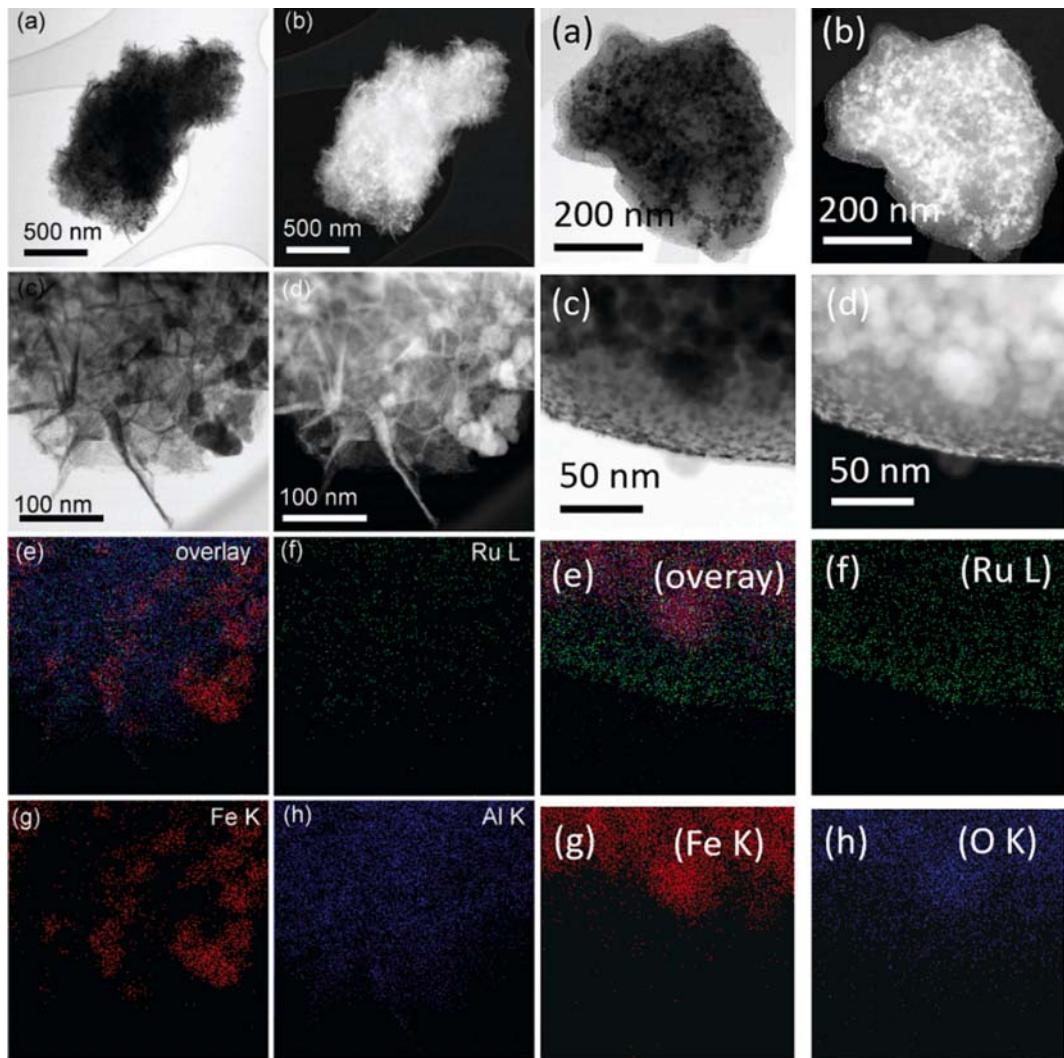


**Fig. 7.** STEM images and EDXS mapping of (left) Ru-Al<sub>2</sub>O<sub>3</sub>-Fe<sub>3</sub>O<sub>4</sub> and (right) Ru-C-Fe<sub>3</sub>O<sub>4</sub> catalysts [32,33].

The effect of induction heating contribution to the overall SAR value, and its dependency on nanoparticle sizes can be observed in Fig. 4 and Fig. 5. Iron, cobalt and nickel were taken into account as mostly used metallic materials in magnetic catalysis. For the model of their induction heating effect comparison, we presumed spherical nanoparticles of 20 nm in diameter. Fig. 4 shows the difference between the total heat exhibited by the 10 nm iron nanoparticles observed by Meffre *et al.* [23] at different frequencies. Higher frequencies also affect the increase in induction heating contribution to the overall heat exhibited by the nanoparticles. However, this contribution is insignificant when compared to the magnetic heating effect for nanoparticles in the observed size range.

A significant difficulty that occurs in magnetically heated systems is the temperature measurement. Although, currently, there is no way to measure the exact surface temperature of the system, the existence of hot spots on the catalyst surface is known. If the reaction is performed in a fixed bed reactor, the temperature of the catalyst surface can be measured accurately. However, if the reaction is performed in a stirred slurry batch reactor system, the temperature sensors measure the temperature of the fluid, and not the catalyst itself. In order to solve this issue, certain measures have been taken, such as synchrotron techniques based on lattice parameters, but these methods are complex and imprecise in case of nanoparticle temperature determination in solution. Díaz-Puerto *et al.* have therefore estimated the nanoparticle surface temperature using the Arrhenius equation [24]. Particle size and

structure are important factors when determining the magnetic heating properties of the material. Larger nanoparticles with higher anisotropy will require higher amplitudes of AMF in order to emit heat [25]. Mille *et al.* report the design and utilization of a setup in order to measure the nanoparticle heating ability using a pyrometer and a double-wall calorimeter. This way, the authors were able to determine temperatures as high as 900 °C [26].

Taking all of the previously mentioned factors into account, we have gathered an overview of the materials used for inductively and magnetically heated catalysts and chemical reaction types enhanced by magnetic heating technologies to shed a light onto this novel method. This is a critical review, where we aim to analyse the advantages of magnetic heating over conventional heating for different catalytic processes, as well as the advantages of different materials used as catalysts and/or heating agents. The gathered literature helps the reader to comprehend different methods of magnetic heating utilization in industrial processes, which shows great green transition potential of this technique. This is exactly why novel research couple it with biomass processing, which would potentially lead to the greater production of alternative fuels, therefore minimizing the large-picture fossil fuel dependency.

In the next chapters, an overview of the magnetic catalysts will be given, as well as the tables with description of their properties and utilization. It is important to note that only the literature with sufficient data on structural and magnetic properties has been gathered into

tables.

## 2. Typical catalysts used in magnetic catalysis

Most of the materials used for this purpose contain magnetic iron oxides, ferrites or other iron compounds. Usually, the used materials are composites consisting of the magnetic part, the support and the catalytically active component as shown in Fig. 6. Since the magnetic nanoparticles may not exhibit suitable surface properties or are highly reactive in an unfavorable way, a recommended solution to that problem is coating the nanoparticles with an inert material [27–29].

### 2.1. Iron-based materials

In order to synthesize different iron materials used in magnetic catalysis, inorganic iron salts are usually used. Aside from the most thoroughly studied iron oxide, other iron compounds are also popular when it comes to magnetic heating, such as ferrites, carbides, iron alloys or even elemental iron. Mehdaoui *et al.* [16] considered various iron-containing samples for hyperthermia measurements in their paper. The authors report that magnetic interactions between the magnetic nanoparticles have a high impact on the SAR value. It has been empirically concluded that larger nanoparticles are better suited for magnetic heating tests. However, since their interactions and behavior are more difficult to foresee, the samples with constant particle size and controlled anisotropy were prepared. This step was crucial since the hysteresis loop shape depends on the anisotropy of the material. Ultimately, it was found that the particles with larger hysteresis loops will have higher SAR values [16].

#### 2.1.1. Iron oxides

Concerning the magnetic materials, iron oxides (specifically magnetite,  $\text{Fe}_3\text{O}_4$  and maghemite,  $\gamma\text{-Fe}_2\text{O}_3$ ) are the most commonly applied ones due to their non-toxicity and the obtained material is usually the mixture of the two. The most simple synthesis route is the co-precipitation of Fe(II) and Fe(III) salts by adding a base to the reaction mixture. This method can be combined with hydrothermal technique to further increase particles size. Gyergyek *et al.* [31] have synthesized the iron oxide nanoparticles using  $\text{Fe}^{2+}$  and  $\text{Fe}^{3+}$  sulphate salts, ammonia and ricinoleic acid which acted as a surfactant. The co-precipitated nanoparticles were of approx. 9 nm in size. Hydrothermal treatment of the precipitate resulted in pronounced growth that could be moderately controlled by addition of ricinolein acid. Authors successfully synthesized magnetic iron oxide nanoparticles having average diameters in the range of 10–80 nm. Nanoparticles smaller than approx. 14 nm demonstrated superparamagnetic behavior while, larger were ferrimagnetic. The study of magnetic heating showed that nanoparticles of average diameter of approx. 20 nm showed highest SAR value 123 kHz. The same authors used magnetic iron oxide nanoparticles to prepare alumina and C nanocomposites which served as a support material to prepare Ru-bearing magnetic catalysts (Fig. 7) [31–33].

Solvothermal method requires careful precursor and surfactant selection. For instance, a paper by Huang *et al.* shows that the synthesis of magnetic materials via solvothermal method resulted in  $\text{Fe}_3\text{O}_4$  microspheres of uniform sizes of about 200 nm composed of fine magnetic core nanocrystals with sizes of about 10 nm [34]. Katugampalage *et al.* [35] coated the  $\text{Fe}_3\text{O}_4$  nanoparticles synthesized by the microwave-assisted solvothermal method in metal-organic framework. The average size of the magnetic nanoparticles was 60 nm and showed cubical/hexagonal shape [35]. Wong *et al.* also report the synthesis of maghemite via co-precipitation method using  $\text{FeCl}_2$  and  $\text{FeCl}_3$ . The maghemite nanoparticles were coated with mesocellular foam, and the synthesized particles exhibited narrow size distribution with average sizes of 8–10 nm [36]. Average maghemite nanoparticle size obtained by Morales *et al.* [21] was 10–12 nm and the maximum SAR value reached was around  $32 \text{ W g}^{-1}$ . Hubbard *et al.* synthesized iron oxide

nanoparticles with average size of around 9 nm with the highest SAR value measured was  $159 \text{ W g}^{-1}$  [37]. Wydra *et al.* obtained the iron oxide nanoparticles by  $\text{FeCl}_2$  and  $\text{FeCl}_3$  co-precipitation without the hydrothermal reaction step. The hydrodynamic particle size was 107 nm, while the measured average SAR value was  $535 \text{ W g}^{-1}$  [38].  $\text{Fe}_3\text{O}_4$  nanoparticles obtained by Lin *et al.* exhibited average sizes of cca. 50 nm and maximum SAR value of  $72.55 \text{ W g}^{-1}$  [39]. Muñoz *et al.* showed the synthesis of maghemite nanoparticles with the average particle size of about 12 nm, while the SAR values were not reported since the heat capacity of the zeolite support was missing [40]. Whajah *et al.* [41] used trisodium citrate as surfactant for the formation of  $\text{Fe}_3\text{O}_4$  microspheres using the method earlier reported by Jiang *et al.* who report the  $\text{Fe}_3\text{O}_4$  nanoparticle formation with the average size of 21 nm, agglomerated into microspheres of around 220 nm [42]. Rivera *et al.* electrochemically synthesized  $\text{Fe}_3\text{O}_4$  nanoparticles with the average size of 21 nm [43]. Gallo Cordova *et al.* performed the synthesis of  $\text{Fe}_3\text{O}_4$  nanoparticles solvothermally in polyol media, producing multicore nanoparticles with average size of 40 nm consisted of small cores of cca. 10 nm in size. The maximum SAR value of the multicore particles was  $850 \text{ W g}^{-1}$  [44]. The preparation of single- and multi-core iron oxide nanoparticles using the microwave assisted polyol technique was also reported by the authors, where the effect of different solvents and heating ramps on the nanoparticle size were shown. The single core nanoparticles exhibited sizes of up to 15 nm, while the size of multicore particles was 60 nm. Single core and multicore particles showed maximum SAR values of about 328 and  $145 \text{ W g}^{-1}$  respectively [45]. Tatarchuk *et al.* [46] reported the synthesis of magnetite via co-precipitation using ferric chloride and ferric sulphate salts with magnetite crystallite sizes of around 14 nm and maximum SAR value of  $14.57 \text{ W g}^{-1}$ . An interesting approach was executed by Danyliuk *et al.* [47] in order to obtain iron oxide particles using fruit extract which act as metal bioreducers from the solutions of metallic salts and stabilizers. Iron oxide nanoparticles have been synthesized using the extracts from two varieties of grapes using grape pulp and grape peel, where formed nanoparticles exhibited crystallite sizes of 14 and 7 nm and maximum SAR values of 1.330 and  $0.488 \text{ W g}^{-1}$  respectively.  $\text{Fe}_3\text{O}_4$  nanoparticles with average sizes of around 17 nm and maximum SAR value of cca.  $270 \text{ W g}^{-1}$  were synthesized using thermal decomposition method with oleic acid acting as ligand by Moura *et al.* [48]. De Cattelle *et al.* reported the synthesis of iron oxide nanoparticles using either poly(ethylene glycol) or oleic acid as stabilizer. Both sets of nanoparticles exhibited average size of about 20 nm [49]. Marten *et al.* synthesized  $\text{Fe}_3\text{O}_4$  nanoparticles via alkaline precipitation, achieving nanoparticles of around 14 nm in size. The nanoparticles were then functionalized with carboxy groups, which lead to agglomeration and the significant increase in hydrodynamic diameter of up to 171 nm [50]. Munoz *et al.* reduced the natural magnetite powder in hydrogen atmosphere and obtained the  $\text{Fe}_3\text{O}_4$  samples with the surface Fe(II)/Fe(III) ratio equal to 0.63. The product nanoparticles were spherical in shape and highly agglomerated with the average diameter of 200 nm. The magnetic properties of the particles were satisfactory, but the specific surface area was quite low, which is a result of its non-porous structure [51]. As an interesting example of magnetic material utilization diversity, a paper from Gómez-Polo *et al.* [52] should be mentioned. They synthesized the  $\text{Fe}_3\text{O}_4\text{-TiO}_2$  composite particles using the magnetic heating of the commercial  $\text{Fe}_3\text{O}_4$  with the average size of 15 nm in order to calcine the  $\text{TiO}_2$  precursor gel [52]. Marques *et al.* describe the synthesis and characterization of magnetite and PU composite. Magnetite nanoparticles were synthesized using the co-precipitation method and showed orthorhombic structure [53]. Yassine *et al.* [54] report the co-precipitation method in iron oxide nanoparticles synthesis whose average diameter was 33 nm. Using the positively charged poly-electrolyte (poly(diallyl dimethyl ammonium chloride)), iron oxide/Au nanoparticles have been synthesized. Since this procedure requires the use of gold nanoparticles, it arises doubt in the scale-up possibilities of the preparation due to the high price of gold. Lee *et al.* [55] prepared the  $\text{Fe}_3\text{O}_4$  nanoparticles by dissolving iron(II) acetylacetone in oleic acid,

**Table 1**  
Properties and utilization of iron oxide materials.

| Magnetic material                        | Synthesis method                       | Average MNP <sup>b</sup> size | SAR / W g <sup>-1</sup> | $f^b$ / kHz | $\mu_0 H$ / mT           | Matrix material                          | Catalytic material            | Reaction                    | Conversion / %     | Selectivity / %   | Ref. |
|--|--|-------------------------------|-------------------------|-------------|--------------------------|--|-------------------------------|-----------------------------|--------------------|-------------------|------|
| Fe <sub>3</sub> O <sub>4</sub>           | Co-precipitation + hydrothermal growth | 15                            | 2.36                    | 280         | 21                       | —  | —                             | —                           | —                  | —                 | [31] |
| Fe <sub>3</sub> O <sub>4</sub>           | Co-precipitation + hydrothermal growth | 24                            | 12.25                   | 123         | 21                       | —  | —                             | —                           | —                  | —                 | [31] |
| Fe <sub>3</sub> O <sub>4</sub>           | Co-precipitation + hydrothermal growth | 20                            | 120                     | 273         | 60                       | $\gamma$ -Al <sub>2</sub> O <sub>3</sub> | Ru                            | Hydrogenation               | 95                 | 92                | [32] |
| Fe <sub>3</sub> O <sub>4</sub>           | Co-precipitation + hydrothermal growth | 17.2                          | n/a                     | 273         | 46                       | C  | Ru                            | Hydrogenation               | 100                | 100               | [33] |
| Fe <sub>3</sub> O <sub>4</sub>           | Solvothermal                           | 200                           | n/a                     | n/a         | C                        | Pd                                       | Suzuki-Miyaura cross-coupling | 100                         | 80.8               | —                 | [34] |
| Fe <sub>3</sub> O <sub>4</sub>           | MW-assisted solvothermal               | 60                            | n/a                     | n/a         | MIL-53 (Al) <sup>c</sup> | MIL-53(Al)                               | OTC <sup>f</sup> adsorption   | 87                          | —                  | —                 | [35] |
| Fe <sub>3</sub> O <sub>4</sub>           | Co-precipitation                       | 9                             | 159                     | 233         | 64.8                     | Oleic acid                               | Oleic acid                    | Polymerization              | 65                 | —                 | [37] |
| Fe <sub>3</sub> O <sub>4</sub>           | Co-precipitation                       | 10                            | 535.5                   | 292         | 75.4                     | —  | —                             | MB <sup>g</sup> degradation | —                  | —                 | [38] |
| Fe <sub>3</sub> O <sub>4</sub>           | Co-precipitation + oxidation           | 11.2                          | 32                      | 331         | 12                       | H-USY zeolite                            | H-USY zeolite                 | —                           | —                  | —                 | [21] |
| $\gamma$ -Fe <sub>2</sub> O <sub>3</sub> | Co-precipitation                       | 50                            | 72.55                   | I = 15 A    | NPC <sup>d</sup>         | NPC                                      | CO <sub>2</sub> adsorption    | 79.2                        | Energy efficiency  | —                 | [39] |
| Fe <sub>3</sub> O <sub>4</sub>           | Co-precipitation                       | 40                            | 850                     | 200         | 21.4                     | —  | —                             | Pollutant degradation       | 90.21 <sup>g</sup> | 74.7 <sup>h</sup> | [44] |
| Fe <sub>3</sub> O <sub>4</sub>           | MW-assisted solvothermal               | 15                            | 328                     | 200         | 30.2                     | —  | —                             | Pollutant degradation       | 100 <sup>g</sup>   | —                 | [45] |
| Fe <sub>3</sub> O <sub>4</sub>           | MW-assisted solvothermal               | 60                            | 145                     | 200         | 30.2                     | —  | —                             | Pollutant degradation       | 100 <sup>g</sup>   | —                 | [45] |
| Fe <sub>3</sub> O <sub>4</sub>           | Dissolution of hematite powder         | 20                            | n/a                     | n/a         | Oleic acid               | Pd                                       | Sonogashira reaction          | 0                           | 0                  | —                 | [49] |
| Fe <sub>3</sub> O <sub>4</sub>           | Dissolution of hematite powder         | 20                            | n/a                     | n/a         | PEG <sup>e</sup>         | Pd                                       | Suzuki cross-coupling         | 87                          | 0                  | —                 | [49] |

<sup>a</sup> Magnetic nanoparticles, <sup>b</sup> Frequency used for magnetic properties determination, <sup>c</sup> A type of metal-organic framework, <sup>d</sup> Nitrogen-doped mesoporous carbon, <sup>e</sup> Polyethylene glycol, <sup>f</sup> oxytetracycline, <sup>g</sup> Decolorization yield, <sup>h</sup> Mineralization yield.

4-biphenyl carboxylic acid and benzyl ether, forming nanoparticles of average size of 21 nm. Magnetic nanoparticles were coated with a hollow silica layer and Pd was added as catalytic material for application in biorthogonal organic synthesis reactions in living cells. However, the feasibility of this process is disputable considering the toxicity of

palladium ions. In order to obtain multicomponent nanomotors, Dhar *et al.* synthesized and tested Fe<sub>2</sub>O<sub>3</sub> and Pd particles on cellulose nanocrystal. The nanomotors were tested and it was observed that the molecules of the composite nanomotor move in the direction of the alternating magnetic field and the maximum SAR value observed for the

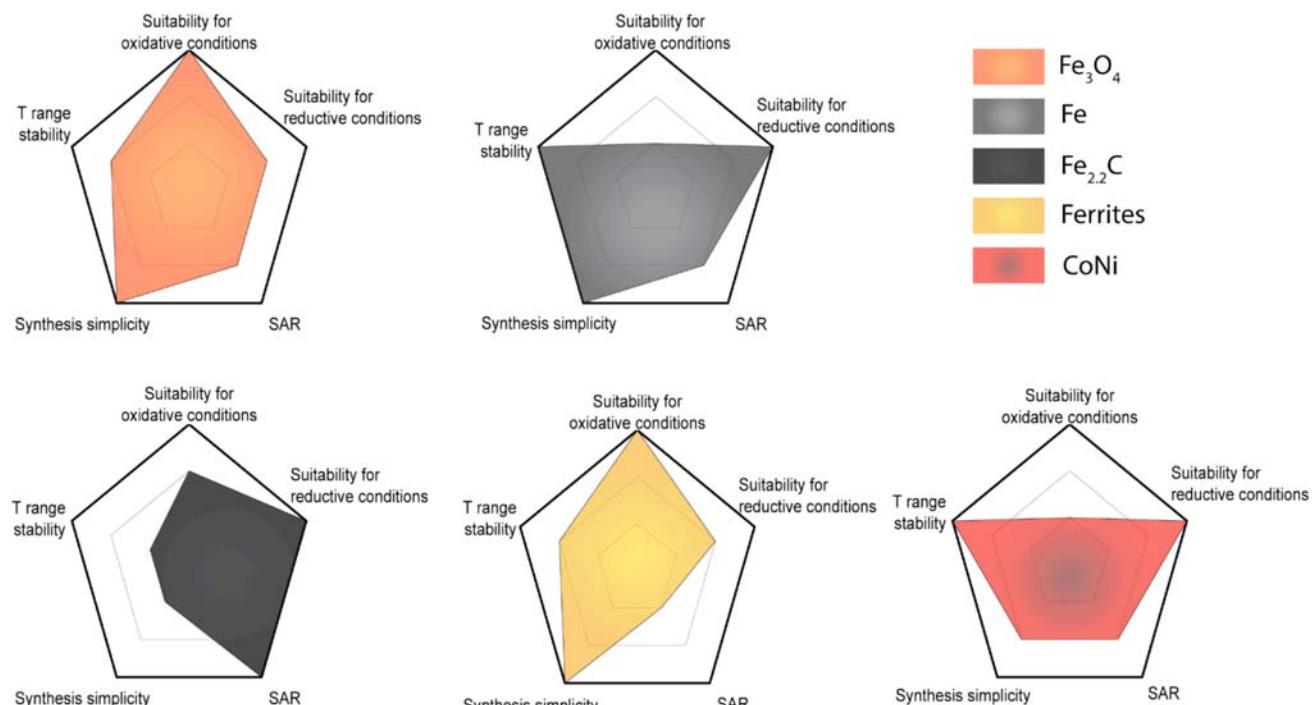


**Fig. 8.** Schematic comparison of the properties of materials commonly used in magnetic catalysis considering their oxidation/reduction stability, average SAR values, synthesis simplicity, and the temperature range stability taking the Curie temperature of the material as the upper temperature limit of application (own work).

**Table 2**  
Properties of Fe magnetic nanoparticles.

| Magnetic material | Synthesis method   | Average MNP size ( <i>d</i> ) / nm | SAR / W/g | f / kHz | $\mu_0 H$ / mT | Matrix material | Catalytic material | Ref. |
|-------------------|--|------------------------------------|-----------|---------|----------------|-----------------|--------------------|------|
| Fe                | from $Fe^{3+}$ solution + thermal decomposition of sugars                          | 25                                 | 70.5      | 477     | 32,7           | C               | Fe-C               | [60] |
| Fe                | from $Fe^{3+}$ solution + thermal decomposition of sugars                          | 70                                 | 32.4      | 477     | 3,7            | C               | Fe-C               | [60] |
| Fe                | from $Fe^{3+}$ solution + thermal decomposition of sugars + hydrothermal synthesis | 54                                 | 760       | 273     | 97             | C               | Fe-C               | [61] |
| Fe                | Organometallic   | 16                                 | 1650      | 300     | 66             | —               | Fe                 | [63] |
| Fe                | Organometallic   | 11                                 | 1300      | 300     | 66             | —               | Fe                 | [63] |
| Fe                | Organometallic   | 11                                 | 284       | 54      | 50             | Fe@Co           | Fe@Co              | [23] |
| Fe                | Organometallic   | 11                                 | 284       | 54      | 50             | Ru              | Fe@Ru              | [23] |

iron oxide/cellulose nanocrystal composite was about  $12 \text{ W g}^{-1}$  [56].

However, iron oxide in core–shell nanoparticles exhibits a certain drawback when it comes to catalyst regeneration conditions. For example, regeneration of coke deposit on the catalyst surface often requires temperatures above  $700^\circ\text{C}$ , which presents a problem, since the Curie temperature of iron oxide is  $622^\circ\text{C}$ . This means that iron oxide nanoparticles inside of the catalyst material would lose their magnetic properties and could not be magnetically heated to the temperature needed for regeneration [2,57]. In addition, transformation to non-magnetic iron oxide might occur at such conditions yielding magnetically inactive material [58]. Properties and performance of iron oxide materials are collected in Table 1.

### 2.1.2. Iron

Considering magnetic heating applications, elemental iron is not an ideal choice. Despite its soft magnetic properties and exhibiting high saturation magnetization, iron in the form of nanoparticles easily undergoes oxidation in air atmosphere, therefore observed nanocomposites mostly contain iron particles in their oxidized forms such as magnetite, maghemite etc. However, zero-valent iron was found to be a good reducing agent for toxic metal ions. In order to reinforce the reducing abilities of iron, as well as reduce its oxygenation tendency, zero-valent iron particles are combined with strong adsorbents such as graphite, activated carbon etc. Hence, some metal materials, such as iron, which cannot withstand even a small amount of oxidation agents in the reaction atmosphere, such as water vapor, and are limited for use in reactions that require reductive conditions (*i.e.* hydrogenation reactions). This limitation is also shown in Fig. 8. Iron nanoparticles used in this work are shown in Table 2. Cervera *et al.* [59] synthesized the Fe-C magnetic nanocomposite using sugars as the carbon source. The nanoparticles synthesized using fructose and glucose exhibited average sizes of about 25 and 70 nm and maximum SAR values of 10 and  $8 \text{ W g}^{-1}$  respectively [59]. Gyergyek *et al.* [60] synthesized carbon coated iron magnetic nanoparticles from formerly synthesized iron oxide nanoparticles [31]. Glucose was used as the carbon source. The obtained material contains elemental iron, iron carbide and iron oxide. The samples differed in annealing temperature and time. Formed iron nanoparticle sizes were between 16 and 54 nm, depending on the annealing conditions and the maximum observed SAR value was 760  $\text{W g}^{-1}$  [60]. Fernández-Veloyos *et al.* [61] 3D printed the commercially obtained zero-valent iron particles with the sizes of about 0,25 mm on polylactic acid support composite. It was observed that, using magnetic induction, the polymer surface remained active for 10 cycles and the polymer material remained almost unchanged. The catalyst reached the maximum temperature of about  $41^\circ\text{C}$  under the magnetic field of 61,8 mT [61].

Zadražil and Štěpánek prepared the Fe microparticles/alumina catalyst using the silica colloidal suspension as binder and used it for the remotely controlled reactions by turning the AMF on and off. The temperature-sensitive reaction of ethanol dehydrogenation was remotely controlled by controlling the power of the alternating magnetic field applied to the system [62]. Furthermore, Mehdaoui *et al.* [63] have reported the multiple step organometallic synthesis route and

characterization of Fe nanocubes of 11 and 16 nm in size. Synthesis was published beforehand by Dumestre *et al.* [64]. Both particle samples' SAR values were tested. The smaller nanoparticles exhibited maximum SAR values of about  $1300 \text{ W g}^{-1}$ , and the larger ones of about  $1650 \text{ W g}^{-1}$  [63]. Meffre *et al.* [23] report the synthesis of nanocomposite Fe@FeCo and Fe@Ru using the adapted organometallic route for iron carbide nanoparticles synthesis [65]. The average nanoparticle sizes of the  $Fe^0$  nanoparticles were between 8 and 12 nm, while the average sizes of the Fe@FeCo and Fe@Ru nanoparticles were 12 and 12.4 nm and the maximum SAR values of 284 and  $190 \text{ W g}^{-1}$  respectively. The nanocomposite particle synthesis method is derived from Fischer-Tropsch mechanism and proceeds through carbonyl substrates on elementary iron seeds [23,65]. Chen *et al.* used iron sponge as the heating core and coated it with carbon using a starch solution. Such material exhibits high porosity, although the particle agglomerates are quite large (microscale agglomerates). This composite was then impregnated by Ni, La and Mn to enable application in catalytic wet peroxide oxidation [66]. Ghosh *et al.* functionalized iron wool with silica coating via sol-gel method and nickel particles and observed that the silica coating acts as a barrier during the  $\text{CO}_2$  hydrogenation reaction and prevents the formation of iron carbide layer on the surface of the iron wool. The maximum SAR value of the iron wool was  $68 \text{ W g}^{-1}$  [67].

### 2.1.3. Iron carbides

The advantages of iron carbide materials in magnetic catalysis are their stability in air and good magnetization properties. Meffre *et al.* proposed the synthesis of iron carbide nanoparticles from zero valent iron nanoparticles with the addition of iron pentacarbonyl ( $Fe(CO)_5$ ). This way the nanocomposite iron/iron carbide particles with the average size of around 13.6 nm were obtained. By controlling the distribution of carbon in the nanocomposite particles, it was possible to finely tune the magnetic anisotropy of the product. The maximum specific absorption rate of the synthesized nanocomposites reached up to  $350 \text{ W g}^{-1}$  [65]. In the work of Asensio *et al.* [11]  $Fe_{2,2}\text{C}$  was prepared via carbidization of zero valent iron and used in combination with Ru, therefore combining exemplary induction heating properties of iron carbide with high catalytic properties of ruthenium which is a popular catalytic hydrogenation/hydrodeoxygenation material. The obtained  $Fe_{2,2}\text{C}$  nanoparticles had an average size of around 14–15 nm and SAR values as high as  $2100 \text{ W g}^{-1}$ , which decreased to  $380 \text{ W g}^{-1}$  after the addition of Ru nanoparticles, which presumably occurred due to ruthenium nanoparticle agglomeration [11]. Niether *et al.* report the utilization of  $Fe_{2,2}\text{C-Ni}$  core–shell particles for water electrolysis via induction heating. Iron carbide particles were produced by the method derived from the Fischer-Tropsch mechanism which includes the presence of mesitylene, CO and  $H_2$  at  $150^\circ\text{C}$  formerly published by Bordet *et al.* [69]. The supplementary data shows that the maximum SAR value of the iron carbide particles equals to about  $3200 \text{ W g}^{-1}$ , while the one for  $Fe_{2,2}\text{C-Ni}$  particles equals to about  $2000 \text{ W g}^{-1}$ , while the average size of the  $Fe_{2,2}\text{C-Ni}$  nanoparticles was 15.2 nm [68]. Kale *et al.* demonstrated a system containing Ni nanoparticles immobilized on SiRALox (a commercial name for silica-alumina oxides) with iron carbide nanoparticles of 14–15 nm in average size as the induction heating

**Table 3**  
Properties and utilization of iron carbide magnetic nanoparticles.

| Magnetic material   | Synthesis method | Average MNP <sup>a</sup> size | SAR / W g <sup>-1</sup> | f <sup>b</sup> / kHz | μ <sub>0</sub> H / mT | Matrix material                         | Catalytic material               | Reaction           | Conversion / % | Selectivity / % | Ref. |
|---------------------|------------------|-------------------------------|-------------------------|----------------------|-----------------------|---|----------------------------------|--------------------|----------------|-----------------|------|
| Fe <sub>2.2</sub> C | Organometallic   | 13.6                          | 350                     | 54                   | 60                    | —                                       | —                                | —                  | —              | —               | [65] |
| Fe <sub>2.2</sub> C | Fe carbidization | 14                            | 2100                    | 96                   | 47                    | —                                       | Ru                               | Hydrodeoxygenation | 100            | 100             | [11] |
| Fe <sub>2.2</sub> C | Organometallic   | 14                            | 2500                    | 100                  | 66                    | CuCr <sub>2</sub> O <sub>5</sub>        | CuCr <sub>2</sub> O <sub>5</sub> | Hydrogenation      | > 99           | > 99            | [70] |
| Fe <sub>2.2</sub> C | Fe carbidization | 14.2                          | 2500                    | 100                  | 47                    | —                                       | Cu                               | Hydrogenation      | > 99           | > 99            | [71] |
| Fe <sub>2.2</sub> C | Fe carbidization | 14                            | 2100                    | 93                   | 47                    | Ni/<br>SiRALO <sub>x</sub> <sup>a</sup> | Ni                               | Methanation        | 96             | 100             | [19] |
| Fe <sub>2.2</sub> C | Fe carbidization | 15                            | 3200                    | 100                  | 47.4                  | Ru/<br>SiRALO <sub>x</sub>              | Ru                               | Methanation        | 86             | 100             | [72] |

<sup>a</sup> Silica-alumina hydrates.

**Table 4**  
Properties and utilization of ferrite-based magnetic nanoparticles.

| Magnetic material                | Synthesis method          | Average MNP <sup>a</sup> size | SAR / W g <sup>-1</sup> | f <sup>b</sup> / kHz | μ <sub>0</sub> H / mT | Matrix material                | Catalytic material  | Reaction                                  | Conversion / %                              | Selectivity / % | Ref. |
|----------------------------------|---------------------------|-------------------------------|-------------------------|----------------------|-----------------------|--------------------------------|---|---|---|-----------------|------|
| NiFe <sub>2</sub> O <sub>4</sub> | Sol-gel                   | ≈ 40                          | 4.7                     | 300                  | 1.5                   | Sulphated TiO <sub>2</sub>     | Sulphated TiO <sub>2</sub>  | Amide synthesis                           | ≈ 30  | —               | [77] |
| CoZn ferrite                     | Sol-gel                   | 5–9                           | 3.95                    | 100                  | n/a                   | —                              | CoZn ferrite  | H <sub>2</sub> O <sub>2</sub> degradation | ≈ 90 <sup>d</sup>                           | —               | [80] |
| CoZn ferrite                     | Sol-gel                   | 12–14                         | 2.56                    | 100                  | 10                    | —                              | CoZn ferrite  | Pb <sup>2+</sup> adsorption               | 23.10 – 289 mg g <sup>-1</sup> <sup>e</sup> | —               | [79] |
| NiFe <sub>2</sub> O <sub>4</sub> | Co-precipitation          | 43 <sup>a</sup>               | 7.4                     | 280                  | n/a                   | Sulphated TiO <sub>2</sub>     | Sulphated TiO <sub>2</sub>  | Amide synthesis-                          | 47 <sup>f</sup>                             | —               | [83] |
| NiZn ferrite                     | Template-assisted sol-gel | 20–120                        | 4.36                    | 295                  | 50                    | —                              | NiZn ferrite  | —   | —   | —               | [85] |
| CoFe <sub>2</sub> O <sub>4</sub> | Co-precipitation          | 24                            | 92.27 <sup>b</sup>      | 337                  | 11.3                  | Fe <sub>3</sub> O <sub>4</sub> | CoFe <sub>2</sub> O <sub>4</sub> + Fe <sub>3</sub> O <sub>4</sub> | —   | —   | —               | [86] |
| CoFe <sub>2</sub> O <sub>4</sub> | Solvothermal reflux       | 10                            | 185.32                  | 316                  | 44.3                  | —                              | CoFe <sub>2</sub> O <sub>4</sub>                                  | —   | —   | —               | [88] |
| NiFe <sub>2</sub> O <sub>4</sub> | Solvothermal reflux       | 11                            | 410                     | 316                  | 44.3                  | —                              | NiFe <sub>2</sub> O <sub>4</sub>                                  | —   | —   | —               | [87] |
| MnFe <sub>2</sub> O <sub>4</sub> | Sonochemical              | 40                            | 139.6                   | 317.8                | 35.6                  | PAN <sup>c</sup>               | PAN   | Pollutant degradation                     | ≈ 85 <sup>g</sup>                           | —               | [89] |
| CoCu ferrite                     | Sol-gel                   | 5.4 – 7.8                     | 83.3                    | 746                  | 20                    | —                              | CoCu ferrite  | —   | —   | —               | [90] |

<sup>a</sup> Crystallite size, <sup>b</sup> SAR value of the composite consisting of Fe<sub>3</sub>O<sub>4</sub> shell which enhances the magnetic properties, <sup>c</sup> Polyacrylonitrile, <sup>d</sup> H<sub>2</sub>O<sub>2</sub> decomposition yield, <sup>e</sup> Adsorption capacity, <sup>f</sup> Amide yield, <sup>g</sup> Degradation yield.

agent. It can be seen that here as well the SAR values of certain samples reached as high as 2100 W g<sup>-1</sup> [19]. It can be deduced that using Fe<sup>0</sup> carbidization synthesis approach of iron carbide nanoparticles, materials with extraordinarily high SAR values can be obtained. Kreissl *et al.* [70] decorated the commercial Cu<sub>2</sub>Cr<sub>2</sub>O<sub>5</sub> with iron carbide nanoparticles which exhibited maximum SAR values of around 2500 W g<sup>-1</sup>, while Lin *et al.* [71] used the two-step organometallic approach in order to produce copper-decorated iron carbide nanoparticles. Although the magnetization after the decoration of the iron carbide sample was somewhat lower than that of pure iron carbide, which exhibited maximum SAR values of about 3200 W g<sup>-1</sup>, SAR of the copper decorated sample still reached values as high as 2500 W g<sup>-1</sup>. The average size of the synthesized iron carbide particles reached around 14 nm [70,71]. Bordet *et al.* synthesized *via* carbidization of Fe<sup>0</sup> nanoparticles, which increases their size from 12.5 to 15.1 nm. After 140 h carbidization process, the iron carbide nanoparticles showed SAR values of 3200 W g<sup>-1</sup> [72]. Bordet *et al.* [73] have reported the attempt to shorten the synthesis time using molecular sieves. Zero-valent iron nanoparticles with average sizes of 9.0 and 12.5 nm were synthesized using previously published methods of organometallic synthesis in hydrogen atmosphere [64,74]. After the carbidization process with and without molecular sieves, the obtained iron carbide nanoparticles exhibited average sizes of 14.0 and 15.1 nm respectively and maximum SAR values of around 3000 and 2700 W g<sup>-1</sup> for iron carbide nanoparticles synthesized from larger Fe<sup>0</sup> particles and around 1700 W g<sup>-1</sup> for the ones synthesized using smaller Fe<sup>0</sup> particles. Therefore, it can be seen that the utilization of molecular sieves somewhat decreases the SAR values of the samples in case of larger zero valent iron nanoparticles carbidization. Molecular

sieves were used in order to extract water from the process to enhance the carbidization reaction according to the Le Chatelier principle. The authors tried to perform carbidization using the mixture of CO<sub>2</sub> and H<sub>2</sub> since CO, which is normally used, is toxic. Without molecular sieves, Fe nanoparticles showed oxidation and coagulation, but the carbidization can be done using CO<sub>2</sub> and H<sub>2</sub> with the extraction of water from the reaction mixture during the process [73]. Table 3 provides information about above-mentioned iron carbide materials and their properties as magnetic heating catalysts.

#### 2.1.4. Ferrites

Cubic spinel ferrites are another popular material which can be used in the manufacture of magnetic catalysts. Properties, composition and feasibility of ferrite are shown in Table 4.

Nickel ferrites have demonstrated the highest activity over other spinel materials due to their high atomic mobility [75]. In that manner, Liu and Rebrov [76] synthesized a composite magnetic catalyst using NiFe<sub>2</sub>O<sub>4</sub> and sulfated titania *via* high energy ball-milling and compared the products with the NiFe<sub>2</sub>O<sub>4</sub>-titania mechanical mixture. The maximum SAR value of the composite material was measured to be 1.7 W g<sup>-1</sup>, while the SAR value of the corresponding mechanical mixture equals 3.1 W g<sup>-1</sup>, which are both lower than the SAR value of the pure nickel ferrite since it is the only compound exhibiting magnetic properties in the mixture. The average grain size of the synthesized samples was between 40 and 50 nm and the catalysts were formed into a pellet [76]. The same group published two papers beforehand where they synthesized the catalyst core-shell NiFe<sub>2</sub>O<sub>4</sub>-TiO<sub>2</sub> nanoparticles *via* sol-gel method, with different contents and ratios of the shell structure.

**Table 5**  
Properties and applications of iron alloy nanoparticles.

| Magnetic material | Synthesis method | Average MNP <sup>a</sup> size | SAR / W g <sup>-1</sup> | f <sup>b</sup> / kHz | μ <sub>0</sub> H / mT | Matrix material | Catalytic material | Reaction           | Conversion / % | Selectivity / % | Ref. |
|-------------------|------------------|-------------------------------|-------------------------|----------------------|-----------------------|-----------------|--------------------|--------------------|----------------|-----------------|------|
| FeNi              | Co-deposition    | 22.3                          | 820                     | 93                   | 47                    | —               | FeNi               | Sabatier reaction  | 100            | 100             | [91] |
| FeNi              | Co-deposition    | 12.4                          | 160                     | 93                   | 47                    | —               | FeNi               | Hydrogenation      | 96             | 100             | [92] |
| FeNi              | Organometallic   | 16                            | 350                     | 93                   | 47                    | —               | FeNi               | Hydrodeoxygenation | 100            | 100             | [93] |
| FeCo              | Organometallic   | 25                            | 1650                    | 100                  | 47                    | —               | FeCo               | Sabatier reaction  | 92.5           | 90              | [94] |
| FeCo              | Organometallic   | 10–11                         | 165 <sup>b</sup>        | 93                   | 25                    | C               | FeCo               | Sabatier reaction  | 96             | 97.5            | [95] |
| FeCo              | Organometallic   | 12.6 <sup>a</sup>             | 700                     | 100                  | 28                    | —               | FeCo               | Hydrogenation      | > 92.5         | 100             | [96] |

<sup>a</sup> Value corresponding to the FeCo@Ni composite.

<sup>b</sup> Value corresponding to the FeCo@C composite.

The particle samples exhibited average sizes of about 50 nm and SAR values between 0.73 and 1.08 W g<sup>-1</sup> [77]. Their paper from 2017. reports the synthesis of a TiO<sub>2</sub>@SiO<sub>2</sub>@NiFe<sub>2</sub>O<sub>4</sub> composite magnetic catalyst particles, where the NiFe<sub>2</sub>O<sub>4</sub> nanoparticles with sizes of 50–70 nm were the core compound, while TiO<sub>2</sub> and SiO<sub>2</sub> were double shell compounds. Sol-gel was used as the synthesis method for the core particles. Properties of the composite samples with and without silica were examined and it was shown that the addition of silica increases the specific surface area of the sample and the SAR value, hence the SAR value of the sample containing silica was 1.5 W g<sup>-1</sup>, while the ones' without silica was 1.1 W g<sup>-1</sup> [78]. Tatarchuk *et al.* [79] published several articles on synthesis, characterization and catalytic testing of ferrite spinels (MFe<sub>2</sub>O<sub>4</sub>) specifically describing cobalt and cobalt-zinc ferrites. In the paper from 2021., they reported a green approach to cobalt-zinc ferrite synthesis, using honey in a combined combustion and sol-gel synthesis method. Fructose and glucose from honey helped the formation of a gel which was then ignited in order to form a nanoscale ferrite powder. The synthesized ferrite nanoparticles exhibited average nanocrystallite sizes of 14 nm and the maximum SLP value of 2.56 W g<sup>-1</sup> [79]. Following the eco-friendly example of honey-supported synthesis, they furtherly synthesized cobalt-zinc ferrite using quince extract *via* sol-gel synthesis. The obtained nanoparticles exhibited crystallite sizes of 4–9 nm and the sample showing maximum measured SAR of 3.95 W g<sup>-1</sup> was Co<sub>0.4</sub>Zn<sub>0.6</sub>Fe<sub>2</sub>O<sub>4</sub> [80]. In the paper from 2023., the same group report the synthesis of cobalt ferrite particles, this time *via* co-precipitation method using Co<sup>2+</sup> and Fe<sup>3+</sup> salts as precursors. The as-synthesized samples show crystallite sizes of about 12 nm, and the annealed samples exhibit crystallite sized of 16 and 18 nm for annealing temperatures of 400 and 600 °C respectively [81]. CoFe<sub>2</sub>O<sub>4</sub> nanoparticles with the average size of 56 nm were synthesized by Ribeiro *et al.* *via* co-precipitation method and coated by ferromagnetic graphite shell by hierarchical co-assembly with the carbon precursors [82]. Houlding *et al.* prepared TiO<sub>2</sub>-NiFe<sub>2</sub>O<sub>4</sub> composite particles *via* mechanochemical synthesis. The NiFe<sub>2</sub>O<sub>4</sub> was obtained *via* sol-gel method and it acted as the magnetic heating material and TiO<sub>2</sub> was used as a support as well as the catalytically active component. The samples showed average crystallite sizes between 35 and 44 nm and the maximum SAR value of 7.4 W g<sup>-1</sup> [83]. Another paper presents ferrite compounds synthesized *via* sol-gel method. The formed Ni-Zn-Pr ferrites and Ni-Zn ferrites have been compared. The average crystallite sizes of the sample were between 24.1 and 91.1 nm and the highest observed magnetic heating rate was 1.65 K s<sup>-1</sup> [84]. Lv *et al.* synthesized Ni<sub>0.5</sub>Zn<sub>0.5</sub>Fe<sub>2</sub>O<sub>4</sub> *via* template assisted sol-gel method as the Ni-Zn ferrite was obtained in the form of microtubes. Crystalline nickel zinc ferrite samples in the range between 25.3 and 112 nm showed maximum SAR value of 4.36 W g<sup>-1</sup> [85]. Borgohain *et al.*, on the other hand, report the synthesis of CoFe<sub>2</sub>O<sub>4</sub> – Fe<sub>3</sub>O<sub>4</sub> composite using the sonic irradiation technique in combination with the reverse co-precipitation method. The prepared composites were also core-shell composites, where CoFe<sub>2</sub>O<sub>4</sub> was the core and the Fe<sub>3</sub>O<sub>4</sub> was the shell component. The nanocomposite samples exhibited nanoparticle sizes of 24 – 50 nm and the maximum observed SAR value was 92.27 W g<sup>-1</sup> [86]. This specific absorption rate value is significantly larger than any other observed in the above-mentioned ferrite materials,

which would probably mean that the Fe<sub>3</sub>O<sub>4</sub> shell had a significant impact on the heating rate of the material. Manohar *et al.* reported the solvothermal reflux synthesis method of cobalt and zinc-nickel ferrites. Both cobalt and zinc-nickel ferrite samples exhibited average particle sizes of about 10 nm and the maximum specific heating rates of the cobalt and zinc-nickel ferrites were 185.32 and 410 W g<sup>-1</sup> respectively, which are higher than those of ferrite nanoparticles synthesized using different methods [87,88]. Since the authors used their approach in order to narrow down the particle size distribution and evidently gotten higher heating rate values, we might assume that the solvothermal method is better for the synthesis of nanostructured magnetic ferrite nanoparticles. Fuentes-García *et al.* reported the synthesis of MnFe<sub>2</sub>O<sub>4</sub> *via* co-precipitation method using ultrasonic laboratory equipment which were then imbedded into the electrospun PAN. The magnetic particles exhibited around 40 nm of average diameter, whereas the size of the final product (fibers) was 760 ± 150 nm. The maximum SLP values of the magnetic nanoparticles and the fibers were 159.4 and 83.7 W g<sup>-1</sup> respectively [89]. Akurati *et al.* described the sol-gel synthesis and characterization of Co-Cu ferrite nanoparticles. The product was synthesized from corresponding nitrate salts in the presence of PEG which acted as a chelating agent. The average particle sizes were in the range between 5.4 – 7.1 nm and increased with the decrease of the ferrite/PEG ratio. The particle sizes increased and the distribution broadened to 9.5 – 98 nm when annealing the samples at higher temperatures. The maximum SAR value observed was 83.3 W g<sup>-1</sup> [90].

### 2.1.5. Iron alloys

Synthesis of FeNi alloy nanoparticles can be done *via* co-decomposition of iron organometallic compounds with the use of palmitic acid as a stabilizer, which is how De Masi *et al.* synthesized FeNi nanoparticles with average sizes of 14.4 – 22.3 nm and SAR values of 200 – 820 W g<sup>-1</sup>, which proves the size dependence of heating abilities in these materials [91]. Raya-Barón *et al.* synthesized FeNi and FeNi@Ni nanoparticles with sizes of 12.5 and 11.9 nm and SAR values of 160 and 93 W g<sup>-1</sup> respectively [92]. Mustieles Marin *et al.* [93] used the described synthesis method to form FeNi particles with the diameter of approximately 16 nm and the maximum SAR value of 350 W g<sup>-1</sup>. Marbaix *et al.* [94] report the synthesis and testing of FeCo alloy nanoparticles. The nanoparticles were also formed *via* decomposition of organometallic Fe and Co compounds. TEM images suggest that the particles are cubic in shape, with average sizes between 10.2 and 22.9 nm and the maximum observed SAR values of 1000–1650 W g<sup>-1</sup>. The nanoparticle sizes decrease with the increase of iron content, while the SAR values are highest for the samples with the greater cobalt content. Martínez-Prieto *et al.* reported the synthesis of FeCo and Co nanoparticles supported on carbon. The carbon layer has a function of preventing the oxidation of FeCo particles in air as well as the protection of the core particles from sintering. Average sizes of the FeCo@C and Co@C nanoparticles were 10.8 and 10.7 nm, with maximum measured SAR values of about 163 and 69 W g<sup>-1</sup> respectively [95]. The same research group report the fabrication FeCo@Ni nanoparticles, where FeCo alloy was the core and Ni the shell of the particle. The average size of the core-shell particles was 12.6 nm, and the maximum SAR value

**Table 6**

Properties and applications of Ni- and Co-based magnetic nanoparticles.

| Magnetic material | Synthesis method          | Average MNP <sup>a</sup> size | SAR / W g <sup>-1</sup> | $f^b$ / kHz | $\mu_0 H$ / mT | Matrix material                          | Catalytic material | Reaction          | Conversion / % | Selectivity / % | Ref.  |
|-------------------|---------------------------|-------------------------------|-------------------------|-------------|----------------|--|--------------------|-------------------|----------------|-----------------|-------|
| NiCo              | Impregnation <sup>a</sup> | 43                            | 280                     | 242         | 28.4           | $\gamma$ -Al <sub>2</sub> O <sub>3</sub> | NiCo               | Methane reforming | 92             | 71              | [106] |
| Ni                | Impregnation <sup>a</sup> | 9                             | 8.16                    | 796         | 20             | FLG/CF <sup>c</sup>                      | Ni                 | Sabatier reaction | 83             | 100             | [108] |
| Co@Ni             | Organometallic            | 11.1                          | 76 <sup>b</sup>         | 93          | 47             | C  | Co@Ni@C            | Sabatier reaction | 74.2           | > 99            | [116] |

<sup>a</sup> Synthesis of nanocomposite, NiCo NPs were impregnated from the precursor solution<sup>b</sup> Value of the Co@Ni@C composite.<sup>c</sup> Few layer graphene/carbon nanofiber.

was around 700 W g<sup>-1</sup>. The core-shell particles were then coated by carbon which ensured the stabilization of the particles, which affected the increase of the average size to 13.8 nm and the drop in maximum SAR value to around 80 W g<sup>-1</sup> [96]. Peng *et al.* demonstrated the electrochemical synthesis route of NiFe/NiFeOOH core-shell particles. Firstly, NiFe was embedded onto the amorphous carbon support *via* pulsed laser deposition which was then combined with rapid thermal annealing. The superparamagnetic core-shell particles were obtained by electrochemical reconstruction [97]. Structure, magnetic properties and feasibility of iron alloys as magnetic catalysts can be seen in Table 5.

## 2.2. Nickel, cobalt and their alloys

Nickel is the most widely used material and many authors use it to substitute iron compounds thanks to its significant magnetic heating abilities. Wang *et al.* [98] employed a mesoporous nickel catalyst which had been supported on activated carbon. The activated carbon had been doped with Ni nanoparticles *via* incipient wetness impregnation, and the average size of the Ni nanoparticles was 4 nm [98,99]. Alumina can also be used as the support for Ni particles. The composite material can be prepared *via* impregnation method. Wang *et al.* report the synthesis of  $\gamma$ -Al<sub>2</sub>O<sub>3</sub>-supported Ni particles [100]. Truong-Phuoc *et al.* described the impregnation of a Ni-catalyst on SiC and estimated the average Ni particle sizes of 13, 21 and 26 nm, for the samples containing 10, 15 and 20 wt% Ni respectively [101]. The same group supported Ni nanoparticles with average size of 12 nm on depleted uranium oxide which was formed from U<sub>3</sub>O<sub>8</sub> powder *via* water spherization and immersed into a Ni salt solution. The uranium oxide phase also plays the role of a heat sinker [102]. Nickel can be used to stabilize reactive metals such as cobalt. Vinum *et al.* used the co-precipitation method to synthesize the CoNi decorated alumina catalyst. The CoNi sample was compared to the sample additionally doped with copper. For both samples, the energy transfer to the process gas was 3 – 20 W g<sup>-1</sup>, while the average particle sizes of CoNi and copper-doped CoNi were 36 and 43 nm [103]. The same group supported CoNi particles with average size of 24 nm on Sm<sub>2</sub>O<sub>3</sub>-Al<sub>2</sub>O<sub>3</sub>, and used the catalyst for steam methane reforming [104]. It was also shown that the co-precipitation method is repeatable and gives similar results considering crystallite and particle sizes, as well as the Curie temperature. Mass-specific magnetization vs. temperature measurement shows that the increase in Co content affects the increase in Curie temperature [105]. Poletto Dotsenko *et al.* report the synthesis of the alloy nanoparticles supported on  $\gamma$ -Al<sub>2</sub>O<sub>3</sub> while changing the Ni/Co ratio and the loading percentage on the alumina support. Ni<sub>50</sub>Co<sub>50</sub> exhibited the highest SAR value of around 280 W g<sup>-1</sup> and the average particle size of 42 nm [106]. Mortensen *et al.* have researched the impregnation of CoNi alloy catalyst on a MgAl<sub>2</sub>O<sub>4</sub>. The samples exhibit average nanoparticle sizes of about 10–12 nm and Curie temperatures of above 800 °C, which is an important property for many endothermic reactions. Magnetic hysteresis losses were found to correspond to the heat generated by the system [107]. Mohanty *et al.* supported Ni particles with carbon nanofiber/few layer graphene *via* wetness impregnation. The average Ni nanoparticle sizes are 8 – 12 nm, depending on the

Ni loading, and the highest measured SAR value for the 10 % Ni loading sample was 8.16 W g<sup>-1</sup> [108]. Nguyen *et al.* researched the Ni-Cu and Cu-Ni-Co catalysts prepared *via* co-precipitation method. The formed catalysts are similar to the grain of rice in shape and show size distribution in the range between 30 and 80 nm. SEM images show that the particles are agglomerated and form chain-like structures [109]. Ni-Co catalysts supported on alumina can also be prepared *via* equilibrium adsorption from the precursors. Scarfiello *et al.* performed the adsorption of Ni-Co nanoparticles on alumina pellets. The particles synthesized under different conditions (Ni/Co ratio, loading, calcination temperature, aging time) exhibit average sizes in the range of about 10 – 40 nm [110]. Varsano *et al.* prepared the Ni-Co alloy using Co chunks and Ni wire inside an arc-melting furnace. Although the calculated crystallite sizes were calculated to be around 15 nm, SEM images have shown that the particles themselves are on the microscale. The highest observed SAR value was around 200 W g<sup>-1</sup> [111,112]. Huang *et al.* [113] used the NiSe<sub>2</sub> alloy as a heating agent with the carbon support. NiSe<sub>2</sub> particles have shown diameter sizes of approximately 3–4 nm and heated rapidly, which boosts the hydrogen evolution reaction time and performance, since the particles were used as an electrocatalyst [113]. Lach *et al.* report the synthesis of various nickel bimetallic catalyst, where Ni mesh or wool was the supporting material combined with nanoscale Au, Pd, Re or Ru. The authors used a multi-step synthesis which includes an intermediate nanoparticle carrier (SiO<sub>2</sub>), which can be easily washed away with NaOH solution after adding a target carrier to the reaction mixture. Average metallic nanoparticle sizes range from 6–12 nm [114,115]. Table 6 shows the properties, utilization and performance of Ni materials as magnetic catalysts.

Similar to nickel, cobalt also finds its use in elementary state in the combination with an appropriate support as well as in alloys [117,118]. For example, cobalt can be used in the form of a thin film as a heating material for catalytic vapor deposition in the combination with the adequate substrate [119]. In their research of single atom catalysts, Gong *et al.* observed atomic cobalt deposited onto a MoS<sub>2</sub> substrate. Laser molecular beam epitaxy was used as the synthesis method for both the substrate and the catalytic material. They report that the magnetic heating in Co/MoS<sub>2</sub> composite, induced *via* alternating magnetic field, is a result of a spin change in the material [120]. On the other hand, Zhou *et al.* reported the utilization of Co-Mn metal-organic framework as catalyst using 2,6-naphthalenedicarboxylate acid as ligand. Their idea was also to use the alternating magnetic field in order to induce the spin flip in the material's active sites so that they could investigate the use of the Co-Mn MOF as an electrocatalyst [118]. Cerezo-Navarette *et al.* synthesized the Co@Ni magnetic nanoparticles encapsulated in C *via* two-step synthesis process which is composed of decomposition and organometallic synthesis procedures. The Co@Ni@C nanoparticles exhibited average sizes of 12.4 nm and a maximum SAR value of about 76 W g<sup>-1</sup>, while the NiCo alloy coated by carbon showed average size of 9.3 nm and the maximum SAR value of about 57 W g<sup>-1</sup> [116]. Both the nanoparticle sizes and their structure differ, so it is difficult to assume which property will affect the SAR value the most.

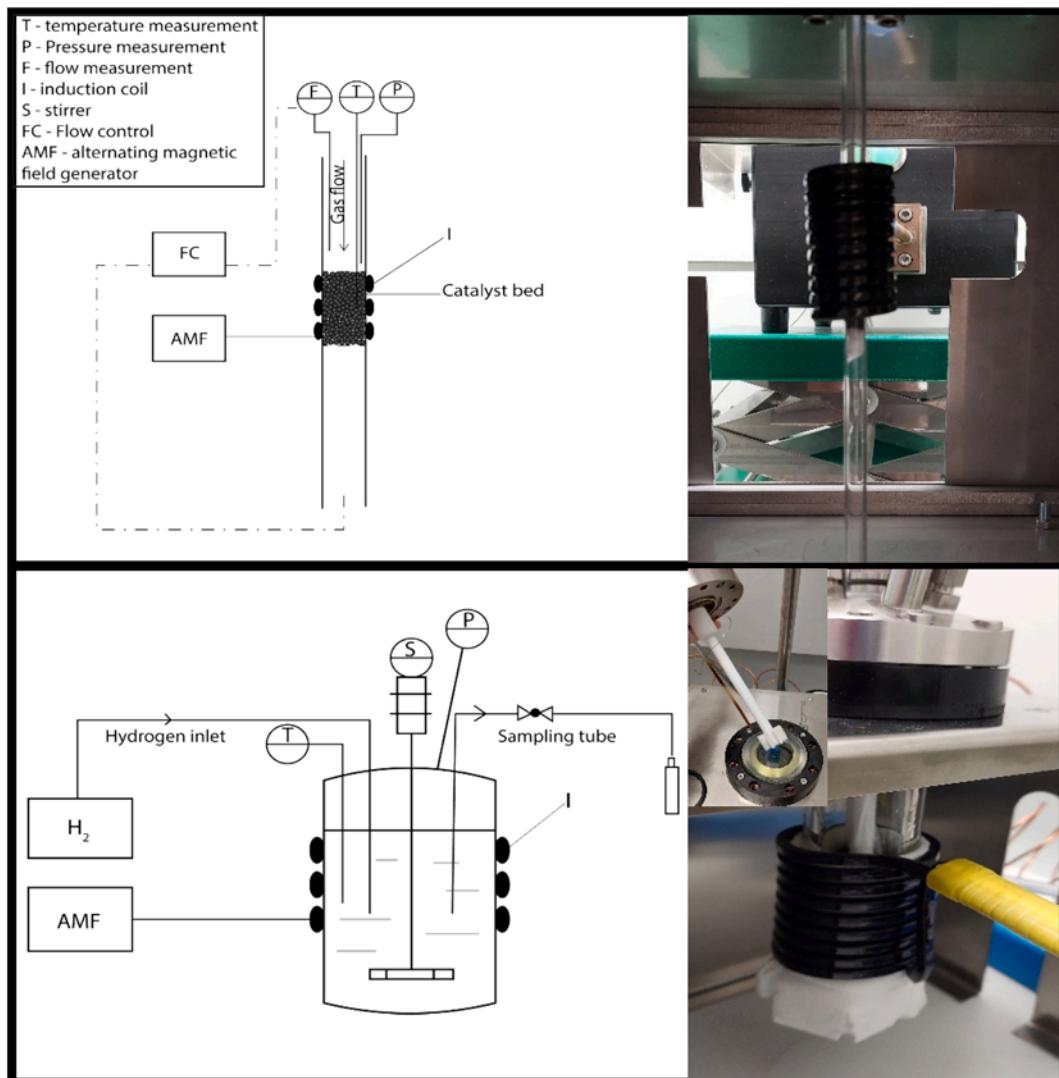


**Fig. 9.** An example of the continuous fixed-bed reactor (up) and a batch slurry-type reactor (down) used for magnetic catalysis (own work).

### 2.3. Other materials

Among the formerly described, most commonly used materials in the field of magnetic heating-assisted catalysis, materials such as copper, aluminum or different metallic oxides can also find their use. Zeng *et al.* [121] showed the synthesis of Gd-doped MoS<sub>2</sub> catalyst *via* laser molecular beam epitaxy (LMBE) method, where the Gd atoms have anchored into the sulfur vacancies on the MoS<sub>2</sub>. It was noted that high-frequency AMF would induce local heating of the catalyst sample, thus increasing its catalytic activity. Since Gd shows low saturation magnetization, there is only a slight temperature rise induced by AMF [121]. Fig. 8 shows a graphic comparison of the different magnetic materials which can be used in magnetic catalysis. This data is meant to facilitate the material choice, considering the most important properties and the application for which they will be used.

### 3. Processes with demonstrated magnetic heating of catalysts

Various reactions have been researched utilizing magnetic heating of the catalyst. In the following subchapters, the results on the most popular magnetically catalyzed reactions will be given.

#### 3.1. Hydrogenation

Considering the current need for green transition and lowering the greenhouse gas emission, it can be claimed that the most popular hydrogenation process today is the CO<sub>2</sub> methanation, *i.e.* Sabatier reaction. Wang *et al.* [98] showed that magnetic heating of Ni/activated C shows the highest CO<sub>2</sub> conversion (ca. 74 %) and CH<sub>4</sub> selectivity (ca. 96 %) at about 370 °C in a flow reactor, while the same values under Joule heating were around 36 and 87 % respectively under the same reaction conditions using a Ni/C catalyst [98], whereas Ni/SiC catalyst shows even larger difference in CO<sub>2</sub> conversion between magnetic heating and Joule heating at 300 °C, although the CH<sub>4</sub> selectivity is 100 % for both mechanisms [101]. The same thing was reported for Ni/SiC catalyst at about 350 °C for 10 % Ni loading. However, when Ni content was increased to 15 %, CO<sub>2</sub> conversion increases at temperatures higher than 360 °C and increases up to about 82 %, which is higher than the maximum conversion under magnetic heating (ca. 80 % for 10 % Ni/SiC) [101]. Similar results have been obtained with Ni on carbon felt catalyst, but at lower temperatures of 320 °C [99]. The same group researched the activity of Ni/γ-Al<sub>2</sub>O<sub>3</sub> for CO<sub>2</sub> hydrogenation and showed over 80 % CO<sub>2</sub> conversion and > 99 % selectivity for CH<sub>4</sub> under temperatures as low as 240 °C [100]. Truong-Phuoc *et al.* achieved 86 % CH<sub>4</sub> yield at just 240 °C using a Ni/uranium oxide catalyst [102]. Mohanty *et al.* obtained similar results for Ni on few layer graphene support at

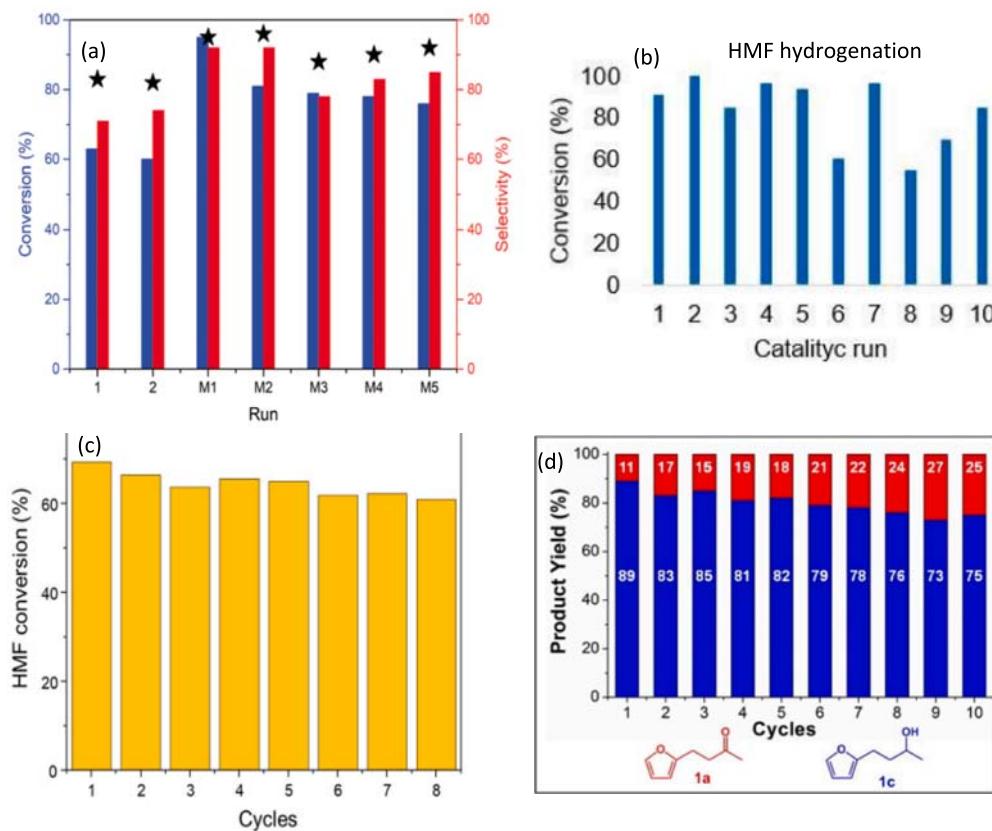


**Fig. 10.** Hydrogenation cycle experiments results for (a) hydrogenation of furfural to furfuryl alcohol [32], (b) [92] (copyright John Wiley and Sons) and (c)[96] (copyright 2022 Americal Chemical Society) HMF hydrogenation to BHMF, and (d)[70], (copyright The authors, Angewandte Chemie International Edition published by Wiley-VCH GmbH) aromatic ketones to aromatic alcohols.

360 °C. Higher temperatures lead to the decrease of conversion and selectivity, which is most likely a result of parallel reactions occurring [108]. It was shown by Bordet *et al.* that the FeC/Ru-SirAlO<sub>x</sub> catalyst can achieve 100 % selectivity to methane and 93 % yield at magnetic field amplitudes as low as 28 mT. Such low AMF amplitudes are usually a sweet spot for magnetic catalysts considering the catalyst stability and energy efficiency of the process [72]. FeCo nanoparticles on Ni/SirAlO<sub>x</sub> showed similar activity, even at lower AMF frequencies and amplitudes, which means that they exhibit better energy efficiency for Sabatier reaction [94]. Martínez-Prieto *et al.* show the Sabatier reaction over FeCo nanoparticles on carbon/Ni. The results show around 95 % CO<sub>2</sub> conversion and about 94 % CH<sub>4</sub> yield at temperatures of about 300 °C [95]. Lach *et al.* report the conversion of CO<sub>2</sub> to methane reaching 99,9 % at 194 °C using a Ru/Ni-wool catalyst in an inductively heated reactor [114]. Bordet *et al.* hydrogenated CO<sub>2</sub> by induction heating of iron carbide nanoparticles. During the reaction, the authors have performed the *in situ* water removal strategy and they found that it enhances the CO<sub>2</sub> conversion and moves increases the selectivity towards the yield of longer-chain hydrocarbons (C<sub>3</sub>H<sub>8</sub>) [73]. De Masi *et al.* achieved total selectivity for CH<sub>4</sub> using FeNi nanoparticle catalyst at lower AMF amplitudes, but struggled with the CO<sub>2</sub> conversion due to the Fe rich catalyst surface. By furtherly depositing Ni nanoparticles on the catalyst surface, they have achieved 100 % CO<sub>2</sub> conversion to CH<sub>4</sub> [91]. Since the green transition implies the transition to alternative energy sources, the attention directed towards biomass has rapidly increased. Gyergyek *et al.* [32] reported successful furfural hydrogenation process using a ruthenium catalyst on γ-Al<sub>2</sub>O<sub>3</sub>-Fe<sub>3</sub>O<sub>4</sub> in a magnetically heated slurry-type reactor. Both continuous flow and batch reactors are shown in Fig. 9. In the first run of the experiment, the conversion of furfural to furfuryl alcohol reached 95 % and the selectivity towards furfuryl

alcohol was close to 100 % at the reaction temperature of about 85 °C, while only 63 % conversion was observed using conventional heating (Fig. 10a) [32].

Raya-Barón *et al.* obtained 98 % conversion of hydroxymethylfurfural to 2,5-bis(hydroxymethyl)furan (BHMF) (Fig. 10b) using magnetic heating during the 15 h of reaction using FeNi nanoparticles with a palmitic acid ligand under magnetic field amplitude of 65 mT and water as solvent, while the FeNi@Ni catalyst with palmitic acid as ligand achieves 96 % selectivity for BHMF in just 6 h under the same reaction conditions [92].

Cerezo-Navarette *et al.* proposed the hydrogenation of benzaldehyde using a FeCo@Ni magnetic catalyst composite, they achieved above 99 % of conversion. The selectivity for toluene, which is a product of total reduction of benzaldehyde, increases with the bulk temperature increase. However, no experiment has shown a 100 % selectivity for one specific product. The product mixture included both benzylalcohol and toluene in different ratios. In case of HMF hydrogenation, the product selectivity is highly dependent on the magnetic field amplitude. At lower magnetic field amplitude (50 mT), the main product was BHMF, while at 83 mT, the main product was dimethylfuran (DMF) since AMF amplitude strongly affects the reaction temperature (Fig. 10c) [96]. Kreissl *et al.* [70] used induction heating of Cu<sub>2</sub>Cr<sub>2</sub>O<sub>5</sub> catalyst decorated with iron carbide nanoparticles to reduce aromatic ketones into aromatic alcohols (Fig. 10d) with conversions of over 99 % under magnetic field amplitudes of both 64 and 80 mT. The reaction could have been performed under mild conditions, with reaction temperature around 80 °C for 17 h [70]. An interesting approach ultimately based on hydrodeoxygenation was proposed by Castellanos-Beltran *et al.* [75], who investigated the use of Ni-ferrite catalyst for the valorization of CO<sub>2</sub> via reverse water-gas shift (RWGS), which implies the conversion of CO<sub>2</sub> into CO in the

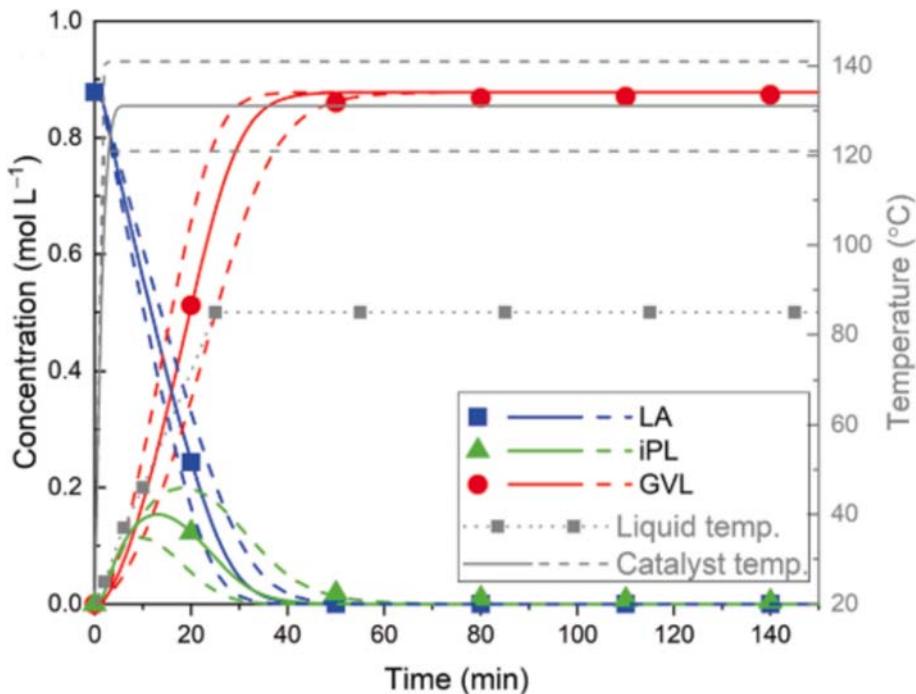


**Fig. 11.** Kinetic modeling of the levulinic acid (LA) hydrogenation in isopropanol using magnetic heating under the hydrogen pressure of 10 bar. (iPL – isopropyl levulinate, GVL –  $\gamma$ -valerolactone)[33].

presence of hydrogen. It was found that the yield of CO is higher in the case of conventional heating for this particular technique. The highest CO yield using conventional heating was 88.1 % at the reaction temperature of 450 °C, while the highest magnetic heating yield was almost 100 % while simultaneously feeding the reactants to the system [75]. Gyergek *et al.* [33] also reported the hydrogenation of levulinic acid to  $\gamma$ -valerolactone, with a 100 % conversion of levulinic acid and a 100 % selectivity towards  $\gamma$ -valerolactone in the first experimental run, both decreasing only by 2 % and 1 % respectively towards the fifth run.

Microkinetic model proposes that, for the liquid temperature of around 80 °C, the corresponding temperature on the catalyst surface is about  $137 \pm 10$  °C (see Fig. 11).

### 3.2. Hydrodeoxygenation (HDO)

Asensio *et al.* describe the attempt of hydrodeoxygenation of aromatic and aliphatic ketones and aldehydes using induction heating. The authors have proven that the induction heating enables the 100 % yield

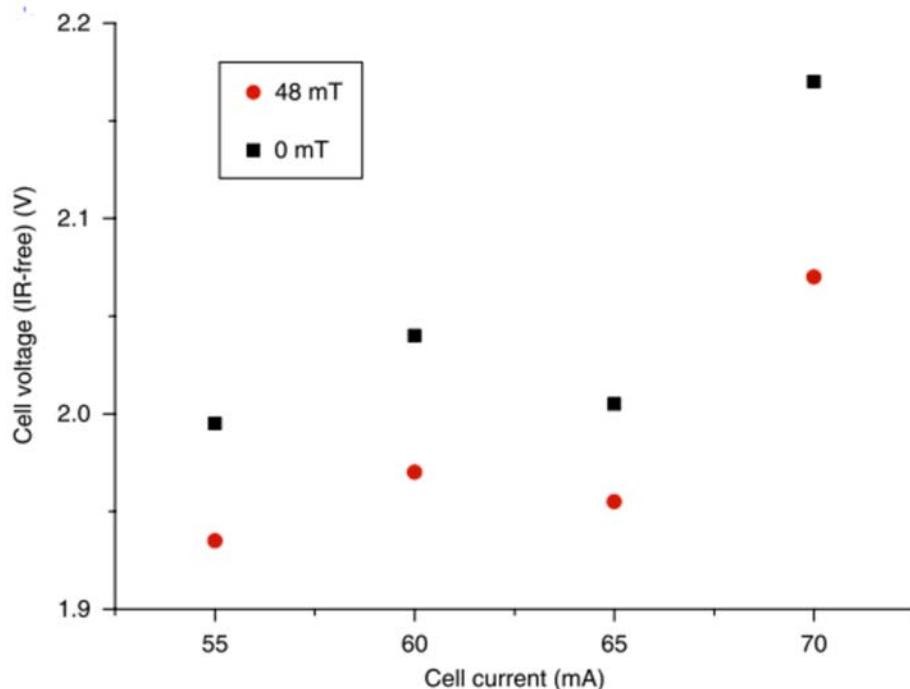


**Fig. 12.** The difference in cell voltage with and without the presence of AMF. Reprinted with permission from reference [68], copyright Springer Nature.

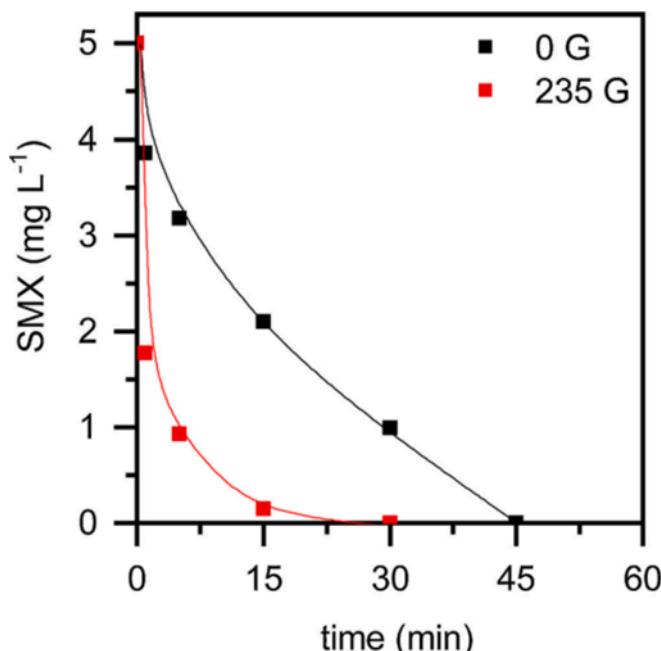


**Fig. 13.** Comparison of sulfamethoxazole concentration drop with and without the application of AMF (235 G = 23.5 mT). Reprinted with permission from reference [51], copyright Elsevier.

of 2-methylfuran (2-MF) from furfural and 2,5-dimethylfuran (DMF) from hydroxymethylfurfural (HMF) using a FeC@Ru catalyst. The AMF amplitude was 58 mT and frequency of 300 kHz in mesitylene, while the reaction lasted 15 h [11]. Mustieles Marin *et al.* [93] describe the inductively heated hydrodeoxygenation process of biomass compounds, including acetophenone, furfural and HMF, using a FeNi@Ni catalyst. Inductively-heated HDO of acetophenone showed a 100 % conversion and selectivity for the expected product, ethylbenzene after the first run and both decrease to 82 % and 66 % respectively after the third run. The authors also managed to execute HDO of furfural and HMF with conversion at 100 % and a 100 % selectivity for methylfuran and 2,5-dimethylfuran respectively after 16 h of reaction in mesitylene. The AMF amplitude was 49 mT and the frequency of 300 kHz [93]. Lin *et al.* also studied the inductively heated HDO of various aromatic aldehydes derived from biomass using a copper decorated iron carbene catalyst. They managed to achieve conversion of over 99 % for all the tested aromatic aldehydes using Cu/iron carbide nanoparticle catalyst. The yield of most of the aromatic alkanes was 99 % and it was lower only in a few examples [71].

### 3.3. Hydrogen evolution reaction (HER) and oxygen evolution reaction (OER)

Induction heating of catalysts can also find its use in electrocatalytic processes, although it is important to note that the accent here is mainly on the energy efficiency expressed in overpotential, and not in conversion or yield percentage. Niether *et al.* [68] claim that heating of electrode material improves the performance of the cell, but, at the same time, increases the risk of severe corrosion. Therefore, using the localized heating of electrodes *via* AMF heating evades the necessity of the whole system to be heated and enhances the HER and OER reactions by supplying enough heat to reduce their overpotential by about 100 and 200 mV respectively. The cell potential with and without AMF can be seen in Fig. 12 [68]. Gong *et al.* have synthesized single atom catalysts by doping cobalt on MoS<sub>2</sub> and utilized AMF for oxygen evolution reaction. The authors claim that the heat produced from the spin polarization flip of the inspected material is responsible for the enhancement of the OER

[120]. The same group of scientists have conducted a similar research employing single atom catalysts for the enhancement of the hydrogen evolution reaction. The material they used was MoS<sub>2</sub> with Gd anchored atoms. Once again, with the effect of local heating of the material induced *via* AMF, the hydrogen evolution reaction was enhanced, thus opening a pathway to increasing the single atom catalyst possibilities with the employment of AMF [121].

### 3.4. Catalytic wet peroxide oxidation

Catalytic wet peroxide oxidation reaction (CWPO) is mainly observed as the model reaction for magnetically heated catalyst testing. Muñoz *et al.* [51], who confirm that the rate constant of the reaction increases with the increase of the magnetic field amplitude. The CWPO of sulfamethoxazole (SMX) was observed as the target compound and was oxidized with H<sub>2</sub>O<sub>2</sub> using magnetite as catalyst. At the same medium temperature, which was roughly 49 °C at the magnetic field amplitude of 235 G, which equals to 23.5 mT. Magnetic induction heating experiment showed almost complete SMX conversion, while the conventional heating method exhibited only 60 % SMX conversion. SMX concentration decrease without and in the presence of AMF can be observed in Fig. 13. The reaction temperature was kept constant throughout the entire experiment [51]. Alcohol oxidation attracts a considerable amount of attention since the products of oxidation of various alcohols can be easily used in further processing. Moura *et al.* observed the effect of surface ligand choice for the catalytic particles on the inductively heated oxidation of 1-octanol to octanal and have compared thermal and inductive heating of the system. It was observed that inductive heating increases the yield of octanal both with and without the Fe<sub>3</sub>O<sub>4</sub> ligand. A 250 % rise in octanal conversion under magnetic heating was observed when the catalyst was treated with pyridine in order to remove the surface ligands. The SLP of the pyridine-treated catalyst also increases by ca. 2.5 times in comparison with the non-treated one. The ligands cause agglomeration of the catalyst, which hinders its activity [48].

### 3.5. Organic synthesis reactions

Organic synthesis reactions are abundant, but there are specific ones on which the magnetic catalysis is tested most frequently. For instance, on the example of Claisen rearrangement reaction, it was concluded that induction heating is more efficient than both oil bath heating and microwave heating [2]. A paper by Ceylan *et al.* depicts a comparison between conventional and induction heating of Suzuki-Miyaura and Heck coupling reactions. Each described reaction shows a larger product yield in the case of induction heating. The used catalyst was silica-coated Fe<sub>2</sub>O<sub>3</sub>/Fe<sub>3</sub>O<sub>4</sub> magnetic nanoparticles, which were heated in a middle-frequency field of 25 kHz [27]. Huang *et al.* [34], on the other hand, report a number of Suzuki-Miyaura cross-coupling reactions and comparing the results while using both induction and Joule heating. It was observed that, in all cases, induction heating results in increased conversion and yield compared to Joule heating. The changing parameters were the catalyst loading, temperature and reactant ratio. The highest observed conversion and yield for the magnetically heated system were equal to 100 and 80.8 % respectively at the reaction temperature of 72 °C and 100 mg of catalyst loading, while, for the same experiment under Joule heating, conversion and yield exhibited values of 83.8 and 74.3 % respectively [34]. Suzuki and Sonogashira induction heated reactions were tested by De Cattelle *et al.* [49]. The highest yield obtained on a Suzuki cross-coupling reaction was 87 %, while the same reaction under conventional heating showed only 8 % conversion. Sonogashira reaction showed 0 % yield, which is supposedly due to low temperatures obtained using their system. Suzuki cross-coupling reactions were performed using Fe<sub>3</sub>O<sub>4</sub>-PEG-Pd catalyst at magnetic field amplitude of 21 mT and frequency of 160 kHz, which resulted in reaction temperature of abou 60 °C [49]. Houlding *et al.* observed the

**Table 7**  
Reactions performed using different magnetic catalysts cited in this work.

| Catalyst  | Reaction type      | Reactant(s)                      | Product(s)                    | Solvent          | T measurement                       | Temperature / °C | Pressure / bar | Reactor system | AMF / mT | f / kHz | Conversion / % | Selectivity / Ref. |
|---|--------------------|----------------------------------|-------------------------------|------------------|-------------------------------------|------------------|----------------|----------------|----------|---------|----------------|--------------------|
| Ni/AC <sup>a</sup>  | Sabatier reaction  | CO <sub>2</sub> , H <sub>2</sub> | CH <sub>4</sub>               | —                | Laser pyrometer, catalyst bed       | 370              | n/a            | Flow           | n/a      | 270     | 74             | 96 [98]            |
| Ni/SiC  | Sabatier reaction  | CO <sub>2</sub> , H <sub>2</sub> | CH <sub>4</sub>               | —                | Laser pyrometer, catalyst bed       | 300              | atm            | Flow           | n/a      | 265     | 79             | 100 [101]          |
| Ni/CF <sup>b</sup>  | Sabatier reaction  | CO <sub>2</sub> , H <sub>2</sub> | CH <sub>4</sub>               | —                | Laser pyrometer, catalyst bed       | 320              | n/a            | Flow           | n/a      | 74      | 97             | [99]               |
| Ni/ $\gamma$ -Al <sub>2</sub> O <sub>3</sub>                                  | Sabatier reaction  | CO <sub>2</sub> , H <sub>2</sub> | CH <sub>4</sub>               | —                | Laser pyrometer, catalyst bed       | 240              | n/a            | Flow           | n/a      | 260     | 85             | 100 [100]          |
| Ni/UO <sub>x</sub>  | Sabatier reaction  | CO <sub>2</sub> , H <sub>2</sub> | CH <sub>4</sub>               | —                | Laser pyrometer, catalyst bed       | 240              | atm            | Flow           | n/a      | 263     | 86             | [102]              |
| Ni/C  | Sabatier reaction  | CO <sub>2</sub> , H <sub>2</sub> | CH <sub>4</sub>               | —                | Laser pyrometer, catalyst bed       | 360              | atm            | Flow           | n/a      | n/a     | 85             | 94 [108]           |
| FeC/Ru-SiAlO <sub>x</sub>   | Sabatier reaction  | CO <sub>2</sub> , H <sub>2</sub> | CH <sub>4</sub>               | —                | IR camera (reactor walls)           | n/a              | atm            | Flow           | 28       | 300     | 93             | 100 [72]           |
| FeCo  | Sabatier reaction  | CO <sub>2</sub> , H <sub>2</sub> | CH <sub>4</sub>               | —                | Pyrometer, catalyst bed             | n/a              | Flow           | 47             | 100      | 92.5    | 90             | [94]               |
| FeCo  | PDR <sup>c</sup>   | CO <sub>2</sub> , H <sub>2</sub> | CO                            | —                | Pyrometer, catalyst bed             | n/a              | Flow           | 60             | 300      | 100     | 42.8           | [94]               |
| FeCo  | MDR <sup>d</sup>   | CO <sub>2</sub> , H <sub>2</sub> | CO                            | —                | Pyrometer, catalyst bed             | n/a              | Flow           | 44             | 300      | 11      | 100            | [94]               |
| FeCo@C  | Sabatier reaction  | CO <sub>2</sub> , H <sub>2</sub> | CH <sub>4</sub>               | —                | Thermocouple in the catalyst bed    | 315              | n/a            | Flow           | 32       | 300     | 96             | 97.5 [95]          |
| FeCo@C  | PDR                | C <sub>3</sub> H <sub>8</sub>    | CO                            | —                | Thermocouple in the catalyst bed    | 620              | n/a            | Flow           | 60       | 300     | 53.6           | 97.2 [95]          |
| FeCo@C  | PDH <sup>e</sup>   | C <sub>3</sub> H <sub>8</sub>    | C <sub>3</sub> H <sub>6</sub> | —                | Thermocouple in the catalyst bed    | 620              | n/a            | Flow           | 65       | 300     | 10.4           | 79.4 [95]          |
| Fe <sub>2</sub> C   | Sabatier reaction  | CO <sub>2</sub> , H <sub>2</sub> | CH <sub>4</sub>               | —                | Optical probe in the reaction fluid | 230              | 3              | Batch          | 35       | 300     | 79             | 56 [73]            |
| FeNi@Ni/SiAlO <sub>x</sub>  | Sabatier reaction  | CO <sub>2</sub> , H <sub>2</sub> | CH <sub>4</sub>               | —                | Pt thermocouple in the catalyst bed | 360              | atm            | Flow           | 22       | 300     | 100            | 100 [91]           |
| Fe <sub>3</sub> O <sub>4</sub> / $\gamma$ -Al <sub>2</sub> O <sub>3</sub> -Ru | Hydrogenation      | Furfural                         | Furfuryl alcohol              | Isopropanol      | IR camera (reactor walls)           | 85               | 10             | Batch          | 30       | 273     | 95             | 92 [32]            |
| FeNi <sub>3</sub> -PA   | Hydrogenation      | Levulinic acid                   | GVL                           | Isopropanol      | Optic probe (reaction fluid)        | 137              | 10             | Batch          | 46       | 273     | 100            | 100 [33]           |
| FeNi <sub>3</sub> -LyS  | Hydrogenation      | HMF                              | BHMF                          | H <sub>2</sub> O | IR camera (reactor walls)           | n/a (below 100)  | 3              | Batch          | 65       | 300     | 98             | 100 [92]           |
| FeCo@Ni   | Hydrogenation      | Levulinic acid                   | GVL                           | H <sub>2</sub> O | IR camera (reactor walls)           | n/a (below 100)  | 3              | Batch          | 65       | 300     | 73             | 89 [92]            |
| FeNi <sub>3</sub> @Ni-LyS   | Hydrodeoxygenation | 4-hydroxyacetophenone            | 4-ethylphenol                 | Dioxane          | IR camera (reactor walls)           | n/a (below 100)  | 3              | Batch          | 65       | 300     | 94             | 85 [92]            |
| FeCo@Ni   | Hydrogenation      | HMF <sup>g</sup>                 | BHMF <sup>h</sup>             | Dioxane          | Optic fiber (reaction fluid)        | 75               | 3              | Batch          | 50       | 300     | 95             | 92.8 [96]          |
| FeCo@Ni   | Hydrogenation      | HMF                              | DMF <sup>i</sup>              | Dioxane          | Optic fiber (reaction fluid)        | 106              | 3              | Batch          | 83       | 300     | >99            | 100 [96]           |
| FeCo@Ni@C   | Hydrogenation      | HMF                              | BHMF                          | H <sub>2</sub> O | Optic fiber (reaction fluid)        | 95               | 3              | Batch          | 100      | 300     | 93.4           | 100 [96]           |
| CuCr <sub>2</sub> O <sub>4</sub> /Fe <sub>2</sub> C                           | Hydrogenation      | Furfuralacetone                  | alpha-methyl-2-furanpropanol  | Heptane          | IR camera (reactor walls)           | 100              | 3              | Batch          | 71       | 350     | >99            | >99 [71]           |
| FeC@Ru  | Hydrodeoxygenation | Furfural                         | 2-methylfuran                 | Mesitylene       | IR camera (reactor walls)           | >165             | 3              | Batch          | 58       | 300     | 100            | 100 [11]           |
| FeC@Ru  | Hydrogenation      | HMF                              | BHMF                          | Mesitylene       | IR camera (reactor walls)           | >166             | 3              | Batch          | 58       | 300     | 100            | 100 [11]           |
| FeNi <sub>3</sub> @Ni   | Hydrodeoxygenation | Acetophenone                     | Ethylbenzene                  | Mesitylene       | IR camera (reactor walls)           | 160-180          | 3              | Batch          | 49       | 300     | 100            | 100 [93]           |
| FeNi <sub>3</sub> @Ni   | Hydrodeoxygenation | HMF                              | DMF                           | Mesitylene       | IR camera (reactor walls)           | 160-180          | 3              | Batch          | 49       | 300     | 100            | 100 [93]           |

(continued on next page)

**Table 7 (continued)**

| Catalyst   | Reaction type           | Reactant(s)                                | Product(s)           | Solvent  | T measurement                     | Temperature / °C | Pressure / bar | Reactor system | AMF / mT | f / kHz | Conversion / % | Selectivity / % | Ref. |
|--|-------------------------|--|----------------------|--|-----------------------------------|------------------|----------------|----------------|----------|---------|----------------|-----------------|------|
| FeNi <sub>3</sub> @Ni                            | Hydrodeoxygenation      | Furfural                                   | 2-methylfuran        | Mesitylene   | IR camera (reactor walls)         | 160–180          | 3              | Batch          | 49       | 300     | 100            | 100             | [93] |
| Cu@FeC   | Hydrogenation           | Benzaldehyde                               | Benzyl alcohol       | Heptane  | IR thermometer (reactor walls)    | 200              | 3              | Batch          | 72       | 350     | >99            | 96              | [71] |
| Cu@FeC   | Hydrodeoxygenation      | Benzaldehyde                               | Toluene              | Heptane  | IR thermometer (reactor walls)    | 105              | 3              | batch          | 72       | 350     | >99            | >99             | [71] |
| NiFe <sub>2</sub> O <sub>4</sub>                 | rWGS <sup>f</sup>       | CO <sub>2</sub>                            | CO                   | —  | Thermocouple in the catalysis bed | 370–440          | —              | Flow           | n/a      | n/a     | >99.9          | >99             | [76] |
| Fe <sub>3</sub> O <sub>4</sub> /SiO <sub>2</sub> | Suzuki-Miyaura coupling | 1-bromo-2-nitrobenzene, phenylboronic acid | 2-phenylbenzonitrile | DMF/H <sub>2</sub> O                                   | IR pyrometer (reactor interior)   | n/a              | —              | Flow           | n/a      | 25      | 83             | 83              | [27] |
| Fe <sub>3</sub> O <sub>4</sub> /SiO <sub>2</sub> | Heck coupling           | 2-iodoanisole, styrene                     | p-styrylanisole      | DMF/H <sub>2</sub> O                                   | IR pyrometer (reactor interior)   | n/a              | —              | Flow           | n/a      | 25      | 84             | 84              | [27] |
| Fe <sub>3</sub> O <sub>4</sub> @C-Pd             | Suzuki-Miyaura coupling | iodobenzene, phenylboronic acid            | Biphenyl             | H <sub>2</sub> O                                       | Thermometer (reaction fluid)      | 72               | n/a            | Batch          | n/a      | n/a     | 100            | 80.8            | [34] |
| Fe <sub>3</sub> O <sub>4</sub> -PEG-Pd           | Suzuki reaction         | 1-bromo-4-nitrobenzene, Phenylboronic acid | Biphenyl             | EtOH/H <sub>2</sub> O + K <sub>2</sub> CO <sub>3</sub> | Temperature of the solution       | 32               | n/a            | Batch          | 16.7     | 160     | 87             | 87              | [49] |
| Fe <sub>3</sub> O <sub>4</sub>                   | Pollutant degradation   | Methylene blue                             | —                    | H <sub>2</sub> O <sub>2</sub>                          | Optical fiber (solution)          | 90               | n/a            | Batch          | 23.9     | 222     | 52.3           | 52.3            | [43] |
| Fe <sub>3</sub> O <sub>4</sub>                   | Pollutant degradation   | Different dyes                             | —                    | H <sub>2</sub> O <sub>2</sub>                          | Optical fiber (solution)          | 90               | n/a            | Batch          | 21.4     | 200     | 90.21          | 74.7            | [44] |

<sup>a</sup> Activated carbon, <sup>b</sup>Carbon felt, <sup>c</sup>Propane dry reforming, <sup>d</sup>Methane dry reforming, <sup>e</sup>Propane dehydrogenation, <sup>f</sup>Reverse water gas shift, <sup>g</sup>Hydroxymethylfurfural, <sup>h</sup>2,5-bis(hydroxymethyl)furan, <sup>i</sup>Dimethylformamide.

catalytic activity of mechanochemically synthesized NiFe<sub>2</sub>O<sub>4</sub>-TiO<sub>2</sub> catalyst for amide yield from 4-phenylbutyric acid and aniline. Sulphated TiO<sub>2</sub> sample exhibited the highest amide yield of up to 50 % conversion at 170 °C [83].

### 3.6. Degradation of pollutants and (plastic) waste

Due to their recyclability, magnetic particles attract increasing amounts of attention when it comes to pollutant removal and degradation [45,89]. Mass and heat phenomena are crucial for the degradation of organic pollutants in wastewater. Mass transport implies the transportation of organic substance and their products through the medium, while the heat transfer regulates the energy balance in order to stabilize the reaction temperature [66]. Rivera *et al.* observed the degradation of methylene blue dye using magnetic induction. They achieved complete discoloration of the sample, although the total organic carbon efficiency turned out to be 52.3 % at around 90 °C, while it showed the value of around 47.5 % for the same temperature experiment performed using a heating bath. It was also concluded that the methylene blue degradation increases with temperature [43]. Fernández-Velázquez *et al.* conducted a research where they compared the effect of thermal bath (conventional heating) and magnetic induction heating in order to oxidize tetracycline at 40 °C using a zero valent iron/PLA composite catalyst. During the first 45 min of the reaction, the highest amount of TC was degraded using magnetic heating, whereas in the next 15 min, conventional heating proved to be more efficient. Zero valent iron/PLA catalyst retains its activity for 10 recycling runs [61]. Gallo-Cordova *et al.* [44] researched the effect of magnetic nanoparticles in wastewater decolorization and mineralization of methyl orange, textile industry wastewater and landfill leachate using iron oxide multicore nanoparticles at magnetic field amplitude of about 21.3 mT and the frequency of 200 kHz. In conventional heating experiments it was shown that the decolorization and mineralization both increase with temperature increase. Magnetic heating experiments exhibited temperatures of 90 °C. Magnetic heating exhibited the highest decolorization and mineralization yields for all of the wastewater samples, especially landfill leachate where decolorization and mineralization yields were 90.21 % and 74.73 % respectively [44]. Table 7 shows reactions performed using various catalytic materials cited in this work.

A promising technique to recycle plastic is the chemical recycling *via* catalytic cracking. In order to deliver the required energy to the process, Morales *et al.* employed magnetic heating. Although the high enough temperatures for the hydrocracking process have not been reached, the authors claim their work a promising pathway towards the catalytic cracking of plastic material [21]. The same research group have published a proof of concept article on the same topic of HDPE degradation *via* hydrocracking. The authors claim that for now, induction heating, in combination with traditional resistive heating, shows promise in plastic recyclability and lowering its impact on the environment [40].

### 4. Potential and timelines of magnetic heating technology

Electrification of processes, especially in biorefining and energy sector can be considered one of the most important leap in green transition. Valorization of various biobased molecules obtained from sugars found in biomass, as stated earlier, leads to the formation of other bio-based compounds used in pharmaceutical industry, oil industry etc. Although conventionally heated reactors for biomass conversion demonstrate high yields, scientists are strongly considering other means of heat delivery to the system in order to furtherly lower carbon emission. It was shown that electrochemical approach of biomass valorization results in a poor selectivity-activity correlation. Microwave heating is a popular method in biomass conversion, but there are certain drawbacks when it comes to the penetration depth of microwaves into the catalytic material and the difficulties considering the process scale-up due to the complexity of the microwave cavity design. As already

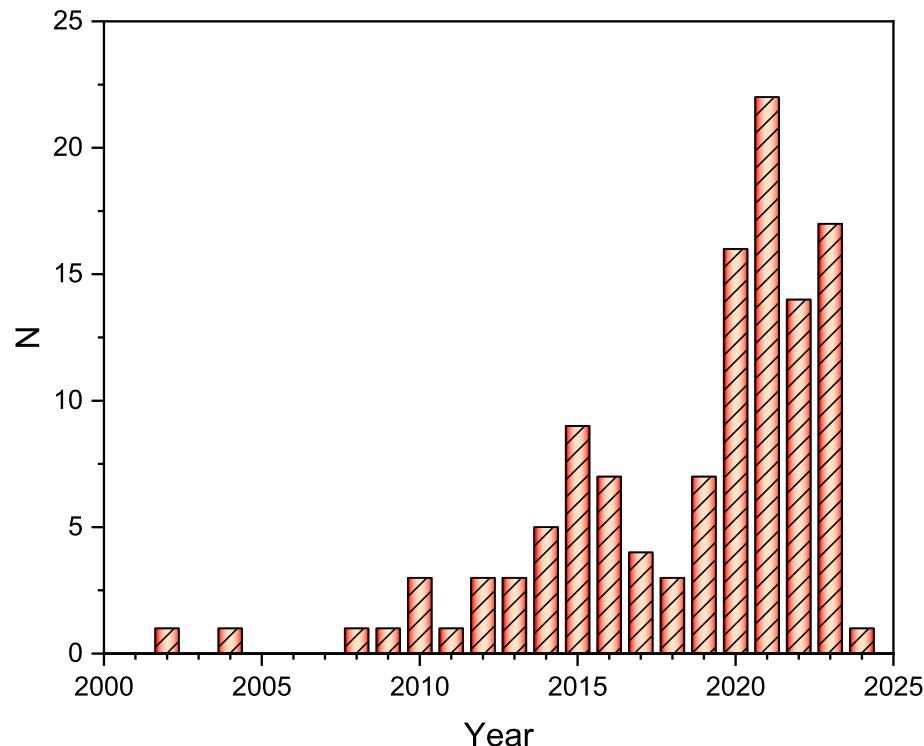


**Fig. 14.** The publishing rate of the articles concerning magnetic heating materials and their utilization in chemical engineering throughout the last couple of decades cited in this paper (N – number of published papers).

mentioned before, the magnetic heating is a way to bring the heat locally to the system, where the temperature on the catalyst hot spots can exceed the solvent boiling point. A thin volume of highly reactive fluid surrounds the magnetically heated catalyst nanoparticles and this is the place where the reaction itself takes place [33]. According to Mustieles Marin *et al.* [93], one of the most promising processes in biomass conversion is the hydrodeoxygenation of furfural and 5-hydroxymethylfurfural (5-HMF), which yield 2-methylfuran (2-MF) and 2,5-dimethylfuran (DMF) respectively. Besides these, lignin was found to be a highly promising source of low-carbon aromatic compounds. Biomass processing encounters difficulties in mass and heat transfer, so there is a significant need for the research and implementation of new catalytic systems which would help to overcome these issues. This is the reason why magnetic catalysis shows an exponential growth in popularity and interest, as can be seen in Fig. 14 and even more papers concerning this topic have been published during the writing of this review paper [93]. The main advantages of magnetic heating are the rapid system responsiveness, the local heat delivery to the catalyst surface, keeping the reaction fluid cooler, since the temperature gradient does not penetrate deep into the mass of the fluid, but instead, there is a thin film of the reaction fluid with the significant temperature gradient. Magnetically heated systems are also safer to use, since the cooldown time of the reaction fluid is short [4], and the ability to quickly Conventionally heated reactors require great amounts of heat brought to the reaction mixture in order to heat up properly, while, in case of magnetic heating, the heat reaches the reaction site directly, which would theoretically affect the drastic decrease in energy consumption [32].

On the other hand, an occurring problem with continuous magnetically heated reactor systems is the axial temperature gradient resulting from the constant heat release from the reactor volume. Chatterjee *et al.* presented a potential solution to this problem and obtained a near-isotherm multi-zone micro-trickle bed reactor. The authors suggest that a multi-zone packed catalyst beds can reduce the axial heat transport throughout the reactor [122]. The same authors claim that a more

accurate approach to determine the temperature gradient is a three-point measuring technique at different positions of the fixed catalyst bed [123].

Additionally, it is important to acknowledge the potential role of artificial intelligence (AI) in magnetically heated chemical processes. Taking into account that this technique is still in its infancy, it is difficult to speak of certain artificial intelligence-supported processes. Nevertheless, some authors propose the potential use of AI in magnetic hyperthermia medical treatments. For example, Osial and Pregowska [124] propose the possible assistance of AI in finding the optimal type and synthesis of magnetic nanoparticles in magnetic hyperthermia, [124] which is probably the most realistic scenario of the AI-assisted magnetic heating process in the near future.

It is certain that valorization of biobased compounds shows great potential and seems as a promising path towards the low-carbon society, but one has to approach the matter at hand critically. As every method and process, magnetic heating also has its drawbacks, the most significant of which is the already mentioned difficult temperature measurement and control, since there is no way to accurately measure the temperature on the catalyst surface yet. This also presents a problem in efforts to model the reaction path and anticipate the development of the process itself. The temperature of the magnetic catalyst suspension can indeed be measured, which can help to a certain extent, but, as written above, the reaction does not happen in the fluid mass, but on the surface of the catalyst. Magnetic heating of nanoparticles also leads to their agglomeration, which can present a problem in long-term activity. Since the prediction of inductively heated reactions is as difficult, the scientists are obligated to learn empirically, while performing an abundance of induction heating experiments under different conditions to get familiar with the effect of parameter change.

## 5. Conclusion

The rate at which a certain chemical process is controlled is of great importance in achieving a carbon neutral society. Time reduction

required to control a process holds a great technical as well as a safety parameter for operators. Among emerging technologies such as electro-catalytic process and plasma assisted process magnetic heating of the catalyst shows rather important advantage. It is a process based on magnetic heating of the catalyst bed meaning that the process is in principle thermo-catalytic. The fast heating of magnetic nanoparticles induces large temperature gradient in vicinity of the catalyst particles, where its surface is at significantly higher temperature than bulk liquid media. This means that the catalytic reaction can proceed at significantly higher rate at comparatively lower bulk fluid temperature when compared to conventional heating. Such heat delivery is especially beneficial to achieve high yields of thermally labile product at significantly shorter time. In comparison to electrocatalytic and plasma assisted process the surface area of the catalyst in contact with substrate is much larger therefore significantly higher yields of desired compound at comparable size of the equipment can be achieved. The relatively broad range of magnetic nanoparticles exhibiting markedly different magnetic and physicochemical properties enables selection of appropriate materials to be realized. When considering reaction conditions to which magnetic nanoparticles will be exposed, ease of their synthesis, use of critical materials and the temperature range to which they need to heat most of the restrictions can be met by existing materials. However, some gaps such as high efficiency of magnetic energy to heat conversion still exist and will have to be addressed in order for the technology to progress to the industrial level. The slower progress on reactor and process design in comparison to the hereby reported development on catalysts material can be for sure ascribed to complexity of the phenomena accompanying magnetic catalysis. Additionally, modern magnetic field generators do not meet the power requirements for the application of magnetic heating in large-scale industrial processes which limits magnetic heating for use in lower-scale processes and “numbering-up” of the processes used in chemical industry. Another interesting not-yet demonstrated application of the magnetic heating is within the electro-thermal fluidized-bed reactor (ETFBR) systems. The ever-advancing fields of multiscale modeling and machine learning are also foreseen as pivotal for understanding the underlying phenomena and for further advancing the magnetically heated catalysis, reactors and the corresponding processes.

#### CRediT authorship contribution statement

**Jakov-Stjepan Pavelić:** Writing – review & editing, Writing – original draft, Methodology, Investigation. **Sašo Gyergyek:** Writing – original draft, Supervision, Methodology, Investigation, Formal analysis, Conceptualization. **Blaz Likozar:** Project administration, Methodology, Funding acquisition. **Miha Grilc:** Writing – review & editing, Writing – original draft, Validation, Supervision, Project administration, Methodology, Investigation, Funding acquisition, Conceptualization.

#### Declaration of competing interest

The authors declare that they have no known competing financial interests or personal relationships that could have appeared to influence the work reported in this paper.

#### Acknowledgments

This research was funded by the Slovenian Research and Innovation Agency (research project N2-0242, programme Scientists4Future and research core fundings P2-0152 and P2-0089). The authors also acknowledge e-CODUCT project funded under Horizon Europe Grant Agreement n°101058100.

#### Data availability

Data will be made available on request.

#### References

- [1] O. Lucia, P. Maussion, E.J. Dede, J.M. Burdio, Induction heating technology and its applications: Past developments, current technology, and future challenges, *IEEE Trans. Ind. Electron.* 61 (2014) 2509–2520, <https://doi.org/10.1109/TIE.2013.2281162>.
- [2] A. Kirschning, L. Kupracz, J. Hartwig, New synthetic opportunities in miniaturized flow reactors with inductive heating, *Chem. Lett.* 41 (2012) 562–570, <https://doi.org/10.1246/cl.2012.562>.
- [3] P. Gao, E.V. Rebrov, T.M.W.G.M. Verhoeven, J.C. Schouten, R. Kleismit, G. Kozlowski, J. Cetnar, Z. Turgut, G. Subramanyam, Structural investigations and magnetic properties of sol-gel Ni 0.5Zn0.5Fe2O4 thin films for microwave heating, *J Appl Phys* 107 (2010), <https://doi.org/10.1063/1.3309767>.
- [4] W. Wang, G. Tuci, C. Duong-Viet, Y. Liu, A. Rossin, L. Luconi, J.M. Nhat, L. Nguyen-Dinh, C. Pham-Huu, G. Giambastiani, Induction Heating: An Enabling Technology for the Heat Management in Catalytic Processes, *ACS Catal.* 9 (2019) 7921–7935, <https://doi.org/10.1021/acscatal.9b02471>.
- [5] R.E. Rosensweig, Heating magnetic fluid with alternating magnetic field, 2002.
- [6] E.L. Verde, G.T. Landi, M.S. Carriao, A.L. Drummond, J.A. Gomes, E.D. Vieira, M. H. Sousa, A.F. Bakuzis, Field dependent transition to the non-linear regime in magnetic hyperthermia experiments: Comparison between maghemite, copper, zinc, nickel and cobalt ferrite nanoparticles of similar sizes, *AIP Adv.* 2 (2012), <https://doi.org/10.1063/1.4739533>.
- [7] J. Carrey, B. Mehdaoui, M. Respaud, Simple models for dynamic hysteresis loop calculations of magnetic single-domain nanoparticles: Application to magnetic hyperthermia optimization, *J. Appl. Phys.* 109 (2011), <https://doi.org/10.1063/1.3551582>.
- [8] I.S. Poperechny, Y.L. Raikher, V.I. Stepanov, Dynamic magnetic hysteresis in single-domain particles with uniaxial anisotropy, *Phys. Rev. B: Condens. Matter Mater. Phys.* 82 (2010), <https://doi.org/10.1103/PhysRevB.82.174423>.
- [9] A.E. Deatsch, B.A. Evans, Heating efficiency in magnetic nanoparticle hyperthermia, *J. Magn. Magn. Mater.* 354 (2014) 163–172, <https://doi.org/10.1016/j.jmmm.2013.11.006>.
- [10] V. Connord, B. Mehdaoui, R.P. Tan, J. Carrey, M. Respaud, An air-cooled Litz wire coil for measuring the high frequency hysteresis loops of magnetic samples - A useful setup for magnetic hyperthermia applications, *Rev. Sci. Instrum.* 85 (2014), <https://doi.org/10.1063/1.4895656>.
- [11] J.M. Asensio, A.B. Miguel, P. Fazzini, P.W.N.M. van Leeuwen, B. Chaudret, Hydrodeoxygenation Using Magnetic Induction: High-Temperature Heterogeneous Catalysis in Solution, *Angew. Chem. Int. Ed.* 58 (2019) 11306–11310, <https://doi.org/10.1002/anie.201904366>.
- [12] Ž. Ponikvar, B. Likozar, S. Gyergyek, Electrification of Catalytic Ammonia Production and Decomposition Reactions: From Resistance, Induction, and Dielectric Reactor Heating to Electrolysis, *ACS Appl. Energy Mater.* (2021), <https://doi.org/10.1021/acsael.1c03045>.
- [13] E. Meloni, G. Iervolino, C. Ruocco, S. Renda, G. Festa, M. Martino, V. Palma, Electrified Hydrogen Production from Methane for PEM Fuel Cells Feeding: A Review, *Energies (basel)* 15 (2022), <https://doi.org/10.3390/en15103588>.
- [14] H. Li, C. Dang, G. Yang, Y. Cao, H. Wang, F. Peng, H. Yu, Bi-functional particles for integrated thermo-chemical processes: Catalysis and beyond, *Particuology* 56 (2021) 10–32, <https://doi.org/10.1016/j.partic.2020.12.002>.
- [15] R. Hudson, Coupling the magnetic and heat dissipative properties of Fe3O4 particles to enable applications in catalysis, drug delivery, tissue destruction and remote biological interfacing, *RSC Adv.* 6 (2016) 4262–4270, <https://doi.org/10.1039/c5ra22260>.
- [16] B. Mehdaoui, R.P. Tan, A. Meffre, J. Carrey, S. Lachaize, B. Chaudret, M. Respaud, Increase of magnetic hyperthermia efficiency due to dipolar interactions in low-anisotropy magnetic nanoparticles: Theoretical and experimental results, *Phys. Rev. B: Condens. Matter Mater. Phys.* 87 (2013), <https://doi.org/10.1103/PhysRevB.87.174419>.
- [17] A. Bordet, W. Leitner, Adaptive Catalytic Systems for Chemical Energy Conversion, *Angew. Chem. Int. Ed.* (2023), <https://doi.org/10.1002/anie.202301956>.
- [18] Y.T. Kim, J.-J. Lee, J. Lee, Electricity-driven reactors that promote thermochemical catalytic reactions via joule and induction heating, *Chem. Eng. J.* 470 (2023) 144333, <https://doi.org/10.1016/j.cej.2023.144333>.
- [19] S.S. Kale, J.M. Asensio, M. Estrader, M. Werner, A. Bordet, D. Yi, J. Marbaix, P. F. Fazzini, K. Soulantica, B. Chaudret, Iron carbide or iron carbide/cobalt nanoparticles for magnetically-induced CO2 hydrogenation over Ni/SiRAIOx catalysts, *Catal. Sci. Technol.* 9 (2019) 2601–2607, <https://doi.org/10.1039/c9cy00437h>.
- [20] J.M. Asensio, J. Marbaix, N. Mille, L.M. Lacroix, K. Soulantica, P.F. Fazzini, J. Carrey, B. Chaudret, To heat or not to heat: A study of the performances of iron carbide nanoparticles in magnetic heating, *Nanoscale* 11 (2019) 5402–5411, <https://doi.org/10.1039/c8nr0235j>.
- [21] I. Morales, M. Muñoz, C.S. Costa, J.M. Alonso, J.M. Silva, M. Multigner, M. Quijorna, M.R. Ribeiro, P. de la Presa, Induction heating in nanoparticle impregnated zeolite, *Materials* 13 (2020), <https://doi.org/10.3390/ma13184013>.
- [22] C. Kuhwald, S. Tiirkhan, A. Kirschning, Inductive heating and flow chemistry – a perfect synergy of emerging enabling technologies, *Beilstein J. Org. Chem.* 18 (2022) 688–706, <https://doi.org/10.3762/bjoc.18.70>.
- [23] A. Meffre, B. Mehdaoui, V. Connord, J. Carrey, P.F. Fazzini, S. Lachaize, M. Respaud, B. Chaudret, Complex nano-objects displaying both magnetic and catalytic properties: A proof of concept for magnetically induced heterogeneous

- catalysis, *Nano Lett.* 15 (2015) 3241–3248, <https://doi.org/10.1021/acs.nanolett.5b00446>.
- [24] Z.J. Díaz-Puerto, Á. Raya-Barón, P.W.N.M. Van Leeuwen, J.M. Asensio, B. Chaudret, Determination of the surface temperature of magnetically heated nanoparticles using a catalytic approach, *Nanoscale* 13 (2021) 12438–12442, <https://doi.org/10.1039/d1nr02283k>.
- [25] N. da Silva Moura, K.R. Bajgiran, A.T. Melvin, K.M. Dooley, J.A. Dorman, Direct Probing of Fe3O4 Nanoparticle Surface Temperatures during Magnetic Heating: Implications for Induction Catalysis, *ACS Appl Nano Mater* 4 (2021) 13778–13787, <https://doi.org/10.1021/acsnanm.1c03168>.
- [26] N. Mille, S. Faure, M. Estrader, D. Yi, J. Marbaix, D. De Masi, K. Soulantica, A. Millán, B. Chaudret, J. Carrey, A setup to measure the temperature-dependent heating power of magnetically heated nanoparticles up to high temperature, *Rev. Sci. Instrum.* 92 (2021), <https://doi.org/10.1063/5.0038912>.
- [27] S. Ceylan, C. Friese, C. Lammel, K. Mazac, A. Kirschning, Inductive heating for organic synthesis by using functionalized magnetic nanoparticles inside microreactors, *Angewandte Chemie - International Edition* 47 (2008) 8950–8953, <https://doi.org/10.1002/anie.200801474>.
- [28] L.M. Rossi, N.J.S. Costa, F.P. Silva, R. Wojcieczak, Magnetic nanomaterials in catalysis: Advanced catalysts for magnetic separation and beyond, *Green Chem.* 16 (2014) 2906–2933, <https://doi.org/10.1039/c4gc00164h>.
- [29] S.R. Chaudhuri, J. Hartwig, L. Kupracz, T. Kodanek, J. Wegner, A. Kirschning, Oxidations of allylic and benzylic alcohols under inductively-heated flow conditions with gold-doped superparamagnetic nanostructured particles as catalyst and oxygen as oxidant, *Adv. Synth. Catal.* 356 (2014) 3530–3538, <https://doi.org/10.1002/adsc.201400261>.
- [30] W. Wu, Z. Wu, T. Yu, C. Jiang, W.S. Kim, Recent progress on magnetic iron oxide nanoparticles: Synthesis, surface functional strategies and biomedical applications, *Sci. Technol. Adv. Mater.* 16 (2015), <https://doi.org/10.1088/1468-6996/16/2/023501>.
- [31] S. Gyergyek, D. Makovec, M. Jagodić, M. Drofenik, K. Schenk, O. Jordan, J. Kovač, G. Dražić, H. Hofmann, Hydrothermal growth of iron oxide NPs with a uniform size distribution for magnetically induced hyperthermia: Structural, colloidal and magnetic properties, *J. Alloy. Compd.* 694 (2017) 261–271, <https://doi.org/10.1016/j.jallcom.2016.09.238>.
- [32] S. Gyergyek, A. Kocjan, M. Grilc, B. Likozar, B. Hočevar, D. Makovec, A hierarchical Ru-bearing alumina/magnetic iron-oxide composite for the magnetically heated hydrogenation of furfural, *Green Chem.* 22 (2020) 5978–5983, <https://doi.org/10.1039/d0gc00966k>.
- [33] S. Gyergyek, M. Grilc, B. Likozar, D. Makovec, Electro-hydrogenation of biomass-derived levulinic acid to  $\gamma$ -valerolactone via the magnetic heating of a Ru nanocatalyst, *Green Chem.* 24 (2022) 2788–2794, <https://doi.org/10.1039/d2gc00102k>.
- [34] C. Huang, Y. Wang, R. Zhong, Z. Sun, Y. Deng, L. Duan, Induction heating enables efficient heterogeneous catalytic reactions over superparamagnetic nanocatalysts, *Chin. Chem. Lett.* 34 (2023), <https://doi.org/10.1016/j.clet.2022.108101>.
- [35] T.R. Katugampalage, C. Ratanatawanate, P. Opaprakasit, C. Kaewsaneha, P. Sreearunothai, A smart magnetically separable MIL-53(Al) MOF-coated nano-adsorbent for antibiotic pollutant removal with rapid and non-contact inductive heat regeneration, *Chemical Engineering Journal Advances* 8 (2021), <https://doi.org/10.1016/j.cej.a.2021.100160>.
- [36] S. Wong, S. Armenise, B.B. Nyakuma, P. Ng, C. Lee, A. Bogush, F. Launay, E. Rebrov, M. Muñoz, Catalytic Pyrolysis of Plastics over Maghemite-Impregnated Mesocellular Foam using Induction Heating, *Chem. Eng. Trans.* 97 (2022) 25–30, <https://doi.org/10.3303/CET2297005>.
- [37] J.W. Hubbard, F. Orange, M.J.F. Guinel, A.J. Guenthner, J.M. Mabry, C. M. Sahagun, C. Rinaldi, Curing of a bisphenol e based cyanate ester using magnetic nanoparticles as an internal heat source through induction heating, *ACS Appl. Mater. Interfaces* 5 (2013) 11329–11335, <https://doi.org/10.1021/am4035575>.
- [38] R.J. Wydra, C.E. Oliver, K.W. Anderson, T.D. Dziubla, J.Z. Hilt, Accelerated generation of free radicals by iron oxide nanoparticles in the presence of an alternating magnetic field, *RSC Adv.* 5 (2015) 18888–18893, <https://doi.org/10.1039/c4ra13564d>.
- [39] X. Lin, B. Shao, J. Zhu, F. Pan, J. Hu, M. Wang, H. Liu, In Situ Electromagnetic Induction Heating for CO<sub>2</sub>Temperature Swing Adsorption on Magnetic Fe3O4/N-Doped Porous Carbon, *Energy Fuel* 34 (2020) 14439–14446, <https://doi.org/10.1021/acs.energyfuels.0c02699>.
- [40] M. Munoz, I. Morales, C.S. Costa, M. Multigner, P. de la Presa, J.M. Alonso, J. M. Silva, M.D.R. Ribeiro, B. Torres, J. Rams, Local induction heating capabilities of zeolites charged with metal and oxide mnps for application in hdp hydrocracking: A proof of concept, *Materials* 14 (2021) 1–15, <https://doi.org/10.3390/ma14041029>.
- [41] B. Whajah, N. Da Silva Moura, J. Blanchard, S. Wicker, K. Gandar, J.A. Dorman, K.M. Dooley, Catalytic Depolymerization of Waste Polyolefins by Induction Heating: Selective Alkane/Alkene Production, *Ind. Eng. Chem. Res.* 60 (2021) 15141–15150, <https://doi.org/10.1021/acs.iecr.1c02674>.
- [42] X. Jiang, F. Wang, W. Cai, X. Zhang, Trisodium citrate-assisted synthesis of highly water-dispersible and superparamagnetic mesoporous Fe3O4 hollow microspheres via solvothermal process, *J. Alloy. Compd.* 636 (2015) 34–39, <https://doi.org/10.1016/j.jallcom.2015.02.156>.
- [43] F.L. Rivera, F.J. Recio, F.J. Palomares, J. Sánchez-Marcos, N. Menéndez, E. Mazarío, P. Herrasti, Fenton-like degradation enhancement of methylene blue dye with magnetic heating induction, *J. Electroanal. Chem.* 879 (2020), <https://doi.org/10.1016/j.jelechem.2020.114773>.
- [44] A. Gallo-Cordova, J.J. Castro, E.L. Winkler, E. Lima, R.D. Zysler, M. del P. Morales, J.G. Ovejero, D.A. Streitwieser, Improving degradation of real wastewaters with self-heating magnetic nanocatalysts, *J Clean Prod* 308 (2021), <https://doi.org/10.1016/j.jclepro.2021.127385>.
- [45] A. Gallo-Cordova, S. Veintemillas-Verdaguer, P. Tartaj, E. Mazarío, M.D. P. Morales, J.G. Ovejero, Engineering iron oxide nanocatalysts by a microwave-assisted polyol method for the magnetically induced degradation of organic pollutants, *Nanomaterials* 11 (2021), <https://doi.org/10.3390/nano11041052>.
- [46] T. Tatarchuk, N. Danyliuk, I. Lapchuk, A. Shylichuk, V. Kotsubynsky, Catalytic activity of magnetite and its magnetic heating properties, *Mater. Today Proc.* 62 (2022) 5805–5811, <https://doi.org/10.1016/j.mtpr.2022.03.494>.
- [47] N. Danyliuk, S. Lischynska, T. Tatarchuk, V. Kotsubynsky, V. Mandzyuk, Magnetite Nanoparticles Synthesized Using Grape Fruit Extract: Synthesis, Morphology, Hyperthermia Application and Catalytic Activity in Hydrogen Peroxide Decomposition, *Physics and Chemistry of Solid State* 23 (2022) 77–88, <https://doi.org/10.15330/pcss.23.1.77-88>.
- [48] N.S. Moura, K.R. Bajgiran, C.L. Roman, L. Daemen, Y. Cheng, J. Lawrence, A. T. Melvin, K.M. Dooley, J.A. Dorman, Catalytic Enhancement of Inductively Heated Fe3O4 Nanoparticles by Removal of Surface Ligands, *ChemSusChem* 14 (2021) 1122–1130, <https://doi.org/10.1002/cssc.202002775>.
- [49] A. De Cattelle, A. Billen, W. Brullot, T. Verbiest, G. Koekelberghs, Magnetically induced Suzuki and Sonogashira reaction performed using recyclable, palladium-functionalized magnetite nanoparticles, *J. Organomet. Chem.* 899 (2019), <https://doi.org/10.1016/j.jorgchem.2019.120905>.
- [50] G.U. Marten, T. Gelbrich, A.M. Schmidt, Hybrid biofunctional nanostructures as stimuli-responsive catalytic systems, *Beilstein J. Org. Chem.* 6 (2010) 922–931, <https://doi.org/10.3762/bjoc.6.98>.
- [51] M. Munoz, J. Nieto-Sandoval, E. Serrano, Z.M. De Pedro, J.A. Casas, CWPO intensification by induction heating using magnetite as catalyst, *J. Environ. Chem. Eng.* 8 (2020), <https://doi.org/10.1016/j.jece.2020.104085>.
- [52] C. Gómez-Polo, S. Larumbe, L.F. Barquín, L.R. Fernández, Magnetic induction heating as a new tool for the synthesis of Fe3O4–TiO2 nanoparticle systems, *J. Nanopart. Res.* 18 (2016), <https://doi.org/10.1007/s11051-016-3426-x>.
- [53] F.D. Marques, M. Nele de Souza, F. Gomes de Souza, Sealing system activated by magnetic induction polymerization, *J. Appl. Polym. Sci.* 134 (2017), <https://doi.org/10.1002/app.45549>.
- [54] S.R. Yassine, Z. Fatfat, G.H. Darwish, P. Karam, Localized catalysis driven by the induction heating of magnetic nanoparticles, *Catal. Sci. Technol.* 10 (2020) 3890–3896, <https://doi.org/10.1039/d0cy00439a>.
- [55] J. Lee, S. Dubbu, N. Kumari, A. Kumar, J. Lim, S. Kim, I.S. Lee, Magnetothermia-Induced Catalytic Hollow Nanoreactor for Bioorthogonal Organic Synthesis in Living Cells, *Nano Lett.* 20 (2020) 6981–6988, <https://doi.org/10.1021/acs.nanolett.0c01507>.
- [56] P. Dhar, S. Narendren, S.S. Gaur, S. Sharma, A. Kumar, V. Katiyar, Self-propelled cellulose nanocrystal based catalytic nanomotors for targeted hyperthermia and pollutant remediation applications, *Int. J. Biol. Macromol.* 158 (2020) 1020–1036, <https://doi.org/10.1016/j.ijbiomac.2020.04.204>.
- [57] J. Zhou, J. Zhao, J. Zhang, T. Zhang, M. Ye, Z. Liu, Regeneration of catalysts deactivated by coke deposition: A review, *Chin. J. Catal.* 41 (2020) 1048–1061, [https://doi.org/10.1016/S1872-2067\(20\)63552-5](https://doi.org/10.1016/S1872-2067(20)63552-5).
- [58] R.M. Cornell, U. Schwertmann, *The Iron Oxides: Structure, Properties, Reactions, Occurrences and Uses*, John Wiley, 2003.
- [59] L. Cervera, J.I. Pérez-Landázabal, E. Garaio, M. Monteserín, S. Larumbe, F. Martín, C. Gómez-Polo, Fe-C nanoparticles obtained from thermal decomposition employing sugars as reducing agents, *J. Alloy. Compd.* 863 (2021), <https://doi.org/10.1016/j.jallcom.2020.158065>.
- [60] S. Gyergyek, E. Chernyshova, K. Boörr, M. Nécemer, D. Makovec, Magnetic carbon nanocomposites via the graphitization of glucose and their induction heating, *J. Alloy. Compd.* 953 (2023), <https://doi.org/10.1016/j.jallcom.2023.170139>.
- [61] S. Fernández-Velayo, J. Sánchez-Marcos, A. Muñoz-Bonilla, P. Herrasti, N. Menéndez, E. Mazarío, Direct 3D printing of zero valent iron@polylactic acid catalyst for tetracycline degradation with magnetically inducing active persulfate, *Sci. Total Environ.* 806 (2022), <https://doi.org/10.1016/j.scitotenv.2021.150917>.
- [62] A. Zadrazil, F. Štepánek, Remote control of reaction rate by radiofrequency heating of composite catalyst pellets, *Chem. Eng. Sci.* 134 (2015) 721–726, <https://doi.org/10.1016/j.ces.2015.05.055>.
- [63] B. Mehdaoui, A. Meffre, L.M. Lacroix, J. Carrey, S. Lachaize, M. Gougeon, M. Respaut, B. Chaudret, Large specific absorption rates in the magnetic hyperthermia properties of metallic iron nanocubes, *J. Magn. Magn. Mater.* 322 (2010), <https://doi.org/10.1016/j.jmmm.2010.05.012>.
- [64] F. Dumestre, B. Chaudret, C. Amiens, P. Renaud, P. Fejes, Superlattices of Iron Nanocubes Synthesized from Fe[N(SiMe<sub>3</sub>)<sub>2</sub>]<sub>2</sub>, *Science* 303 (2004) 821–823, <https://doi.org/10.1126/science.1092641>.
- [65] A. Meffre, B. Mehdaoui, V. Kelsen, P.F. Fazzini, J. Carrey, S. Lachaize, M. Respaut, B. Chaudret, A simple chemical route toward monodisperse iron carbide nanoparticles displaying tunable magnetic and unprecedented hyperthermia properties, *Nano Lett.* 12 (2012) 4722–4728, <https://doi.org/10.1021/nl302160d>.
- [66] H. Chen, J. Lee, Y. Zheng, Q. Duan, A non-traditional energy transfer process in CWPO heterogeneous reaction for wastewater treatment, *Chem. Eng. Res. Des.* 114 (2016) 142–147, <https://doi.org/10.1016/j.cherd.2016.08.020>.
- [67] S. Ghosh, T. Ourlin, J. Mazarío, S. Cayez, S. Daccache, J. Carrey, B. Chaudret, Fe@SiO<sub>2</sub>@Ni: An Iron-Based Composite Material for Magnetically Induced Hydrogenation Reactions in Gas and Solution Phases, *Chem. Mater.* 35 (2023) 7542–7553, <https://doi.org/10.1021/acs.chemmater.3c01118>.

- [68] C. Niether, S. Faure, A. Bordet, J. Deseure, M. Chatenet, J. Carrey, B. Chaudret, A. Rouet, Improved water electrolysis using magnetic heating of FeC-Ni core-shell nanoparticles, *Nat. Energy* 3 (2018) 476–483, <https://doi.org/10.1038/s41560-018-0132-1>.
- [69] A. Bordet, L.M. Lacroix, K. Soulantica, B. Chaudret, A New Approach to the Mechanism of Fischer-Tropsch Syntheses Arising from Gas Phase NMR and Mass Spectrometry, *ChemCatChem* 8 (2016) 1727–1731, <https://doi.org/10.1002/cetc.201600245>.
- [70] H. Kreissl, J. Jin, S.H. Lin, D. Schütté, S. Störte, N. Levin, B. Chaudret, A. J. Vorholt, A. Bordet, W. Leitner, Commercial Cu<sub>2</sub>Cr<sub>2</sub>O<sub>5</sub> Decorated with Iron Carbide Nanoparticles as a Multifunctional Catalyst for Magnetically Induced Continuous-Flow Hydrogenation of Aromatic Ketones, *Angewandte Chemie - International Edition* 60 (2021) 26639–26646, <https://doi.org/10.1002/anie.202107916>.
- [71] S.H. Lin, W. Hetaba, B. Chaudret, W. Leitner, A. Bordet, Copper-Decorated Iron Carbide Nanoparticles Heated by Magnetic Induction as Adaptive Multifunctional Catalysts for the Selective Hydrodeoxygenation of Aldehydes, *Adv. Energy Mater.* 12 (2022), <https://doi.org/10.1002/aenm.202201783>.
- [72] A. Bordet, L.-M. Lacroix, P.-F. Fazzini, J. Carrey, K. Soulantica, B. Chaudret, Magnetically Induced Continuous CO 2 Hydrogenation Using Composite Iron Carbide Nanoparticles of Exceptionally High Heating Power, *Angew. Chem.* 128 (2016) 16126–16130, <https://doi.org/10.1002/ange.201609477>.
- [73] A. Bordet, J.M. Asensio, K. Soulantica, B. Chaudret, Enhancement of Carbon Oxides Hydrogenation on Iron-Based Nanoparticles by In-Situ Water Removal, *ChemCatChem* 10 (2018) 4047–4051, <https://doi.org/10.1002/cetc.201800821>.
- [74] L.M. Lacroix, S. Lachaize, A. Falqui, M. Respaud, B. Chaudret, Iron nanoparticle growth in organic superstructures, *J. Am. Chem. Soc.* 131 (2009) 549–557, <https://doi.org/10.1021/ja805719c>.
- [75] I.J. Castellanos-Beltran, L.S. Perreault, N. Braidy, Application of Ni-Spinel in the Chemical-Looping Conversion of CO<sub>2</sub> to CO via Induction-Generated Oxygen Vacancies, *J. Phys. Chem. C* 125 (2021) 7213–7226, <https://doi.org/10.1021/acs.jpcc.1c00928>.
- [76] Y. Liu, E.V. Rebrov, Direct amide synthesis over composite magnetic catalysts in a continuous flow reactor, *Catalysts* 11 (2021) 1–11, <https://doi.org/10.3390/catal11020146>.
- [77] Y. Liu, P. Gao, N. Cherkasov, E.V. Rebrov, Direct amide synthesis over core-shell TiO<sub>2</sub>@NiFe2O4 catalysts in a continuous flow radiofrequency-heated reactor, *RSC Adv.* 6 (2016) 100997–101007, <https://doi.org/10.1039/c6ra22659k>.
- [78] Y. Liu, N. Cherkasov, P. Gao, J. Fernández, M.R. Lees, E.V. Rebrov, The enhancement of direct amide synthesis reaction rate over TiO<sub>2</sub>@SiO<sub>2</sub>@NiFe2O4 magnetic catalysts in the continuous flow under radiofrequency heating, *J. Catal.* 355 (2017) 120–130, <https://doi.org/10.1016/j.jcat.2017.09.010>.
- [79] T. Tatarchuk, A. Shylichuk, Z. Sojka, J. Grybos, M. Naushad, V. Kotsubynsky, M. Kowalska, S. Kwiatkowska-Marks, N. Danyliuk, Green synthesis, structure, cations distribution and bonding characteristics of superparamagnetic cobalt-zinc ferrites nanoparticles for Pb(II) adsorption and magnetic hyperthermia applications, *J. Mol. Liq.* 328 (2021), <https://doi.org/10.1016/j.molliq.2021.115375>.
- [80] T. Tatarchuk, N. Danyliuk, V. Kotsubynsky, A. Shumskaya, E. Kaniukov, A. A. Ghfar, M. Naushad, A. Shylichuk, Eco-friendly synthesis of cobalt-zinc ferrites using quince extract for adsorption and catalytic applications: An approach towards environmental remediation, *Chemosphere* 294 (2022), <https://doi.org/10.1016/j.chemosphere.2022.133565>.
- [81] T. Tatarchuk, A. Shylichuk, N. Danyliuk, M. Naushad, V. Kotsubynsky, V. Boychuk, Cobalt ferrite as an electromagnetically boosted metal oxide hetero-Fenton catalyst for water treatment, *Chemosphere* 326 (2023), <https://doi.org/10.1016/j.chemosphere.2023.138364>.
- [82] R.S. Ribeiro, J. Gallo, M. Bañobre-López, A.M.T. Silva, J.L. Faria, H.T. Gomes, Enhanced performance of cobalt ferrite encapsulated in graphitic shell by means of AC magnetically activated catalytic wet peroxide oxidation of 4-nitrophenol, *Chem. Eng. J.* 376 (2019), <https://doi.org/10.1016/j.cej.2018.09.173>.
- [83] T.K. Houlding, P. Gao, V. Degirmenci, K. Tchabanenko, E.V. Rebrov, Mechanochemical synthesis of TiO<sub>2</sub>/NiFe2O4 magnetic catalysts for operation under RF field, *Mater Sci Eng B Solid State Mater Adv Technol* 193 (2015) 175–180, <https://doi.org/10.1016/j.msrb.2014.12.011>.
- [84] B. Yan, P.Z. Gao, Z.L. Lu, R.X. Ma, E.V. Rebrov, H.B. Zheng, Y.X. Gao, Effect of Pr<sub>3</sub> + substitution on the microstructure, specific surface area, magnetic properties and specific heating rate of Ni<sub>0.5</sub>Zn<sub>0.5</sub>Pr<sub>x</sub>Fe<sub>2-x</sub>O<sub>4</sub> nanoparticles synthesized via sol-gel method, *J Alloys Compd* 639 (2015) 626–634, <https://doi.org/10.1016/j.jallcom.2015.03.211>.
- [85] H.N. Lv, E.V. Rebrov, P.Z. Gao, R.X. Ma, Z.L. Lu, J. Xu, Controllable synthesis of one-dimensional isolated Ni<sub>0.5</sub>Zn<sub>0.5</sub>Fe<sub>2</sub>O<sub>4</sub> microtubes for application as catalyst support in RF heated reactors, *Ceram. Int.* 42 (2016) 7793–7802, <https://doi.org/10.1016/j.ceramint.2016.01.214>.
- [86] C. Borgohain, J.P. Borah, CoFe<sub>2</sub>O<sub>4</sub>-Fe<sub>3</sub>O<sub>4</sub> bimagnetic heterostructure: A versatile core-shell nanoparticle with magnetically recoverable photocatalytic and self heating properties, *Mater. Res. Express* 7 (2020), <https://doi.org/10.1088/2053-1591/ab6493>.
- [87] A. Manohar, K. Chintagumpala, K.H. Kim, Mixed Zn-Ni spinel ferrites: Structure, magnetic hyperthermia and photocatalytic properties, *Ceram. Int.* 47 (2021) 7052–7061, <https://doi.org/10.1016/j.ceramint.2020.11.056>.
- [88] A. Manohar, D.D. Geleta, C. Krishnamoorthi, J. Lee, Synthesis, characterization and magnetic hyperthermia properties of nearly monodisperse CoFe<sub>2</sub>O<sub>4</sub> nanoparticles, *Ceram. Int.* 46 (2020) 28035–28041, <https://doi.org/10.1016/j.ceramint.2020.07.298>.
- [89] J.A. Fuentes-García, B. Sanz, R. Mallada, M.R. Ibarra, G.F. Goya, Magnetic nanofibers for remotely triggered catalytic activity applied to the degradation of organic pollutants, *Mater. Des.* 226 (2023), <https://doi.org/10.1016/j.matdes.2023.111615>.
- [90] R.R. Akurati, N.K. Jaladi, S.R. Kurapati, G. Kapusetti, M. Choppadandi, P. Mandal, Preparation, characterization and study of magnetic induction heating of Co-Cu nanoparticles, *Mater. Today Commun.* 34 (2023), <https://doi.org/10.1016/j.mtcomm.2022.104964>.
- [91] D. De Masi, J.M. Asensio, P. Fazzini, L. Lacroix, B. Chaudret, Engineering Iron–Nickel Nanoparticles for Magnetically Induced CO 2 Methanation in Continuous Flow, *Angew. Chem.* 132 (2020) 6246–6250, <https://doi.org/10.1002/ange.201913865>.
- [92] Á. Raya-Barón, J. Mazarío, G. Mencia, P.F. Fazzini, B. Chaudret, l-Lysine Stabilized FeNi Nanoparticles for the Catalytic Reduction of Biomass-Derived Substrates in Water Using Magnetic Induction, *ChemSusChem* 16 (2023), <https://doi.org/10.1002/cssc.202300009>.
- [93] I. Mustieles Marin, D. De Masi, L.M. Lacroix, P.F. Fazzini, P.W.N.M. van Leeuwen, J.M. Asensio, B. Chaudret, Hydrodeoxygenation and hydrogenolysis of biomass-based materials using FeNi catalysts and magnetic induction, *Green Chem.* 23 (2021), <https://doi.org/10.1039/d0gc03495a>.
- [94] J. Marbaix, N. Mille, L.M. Lacroix, J.M. Asensio, P.F. Fazzini, K. Soulantica, J. Carrey, B. Chaudret, Tuning the Composition of FeCo Nanoparticle Heating Agents for Magnetically Induced Catalysis, *ACS Appl. Nano Mater.* 3 (2020) 3767–3778, <https://doi.org/10.1021/acsnano.0c00444>.
- [95] L.M. Martínez-Prieto, J. Marbaix, J.M. Asensio, C. Cerezo-Navarrete, P.F. Fazzini, K. Soulantica, B. Chaudret, A. Corma, Ultrastable Magnetic Nanoparticles Encapsulated in Carbon for Magnetically Induced Catalysis, *ACS Appl. Nano Mater.* 3 (2020) 7076–7087, <https://doi.org/10.1021/acsnano.0c01392>.
- [96] C. Cerezo-Navarrete, I.M. Marin, H. García-Miquel, A. Corma, B. Chaudret, L. M. Martínez-Prieto, Magnetically Induced Catalytic Reduction of Biomass-Derived Oxygenated Compounds in Water, *ACS Catal.* 12 (2022) 8462–8475, <https://doi.org/10.1021/acscatal.2c01696>.
- [97] D. Peng, C. Hu, X. Luo, J. Huang, Y. Ding, W. Zhou, H. Zhou, Y. Yang, T. Yu, W. Lei, C. Yuan, Electrochemical Reconstruction of NiFe/NiFeOOH Superparamagnetic Core/Catalytic Shell Heterostructure for Magnetic Heating Enhancement of Oxygen Evolution Reaction, *Small* 19 (2023), <https://doi.org/10.1002/smll.202205665>.
- [98] W. Wang, C. Duong-Viet, L. Truong-Phuoc, J.M. Nhut, L. Vidal, C. Pham-Huu, Activated carbon supported nickel catalyst for selective CO<sub>2</sub> hydrogenation to synthetic methane under contactless induction heating, *Catal. Today* 418 (2023), <https://doi.org/10.1016/j.cattod.2023.114073>.
- [99] W. Wang, C. Duong-Viet, Z. Xu, H. Ba, G. Tuci, G. Giambastiani, Y. Liu, T. Truong-Huu, J.M. Nhut, C. Pham-Huu, CO<sub>2</sub> methanation under dynamic operational mode using nickel nanoparticles decorated carbon felt (Ni/OCF) combined with inductive heating, *Catal. Today* 357 (2020) 214–220, <https://doi.org/10.1016/j.cattod.2019.02.050>.
- [100] W. Wang, C. Duong-Viet, G. Tuci, Y. Liu, A. Rossin, L. Luconi, J.M. Nhut, L. Nguyen-Dinh, G. Giambastiani, C. Pham-Huu, Highly Nickel-Loaded γ-Alumina Composites for a Radiofrequency-Heated, Low-Temperature CO<sub>2</sub> Methanation Scheme, *ChemSusChem* 13 (2020) 5468–5479, <https://doi.org/10.1002/cssc.202001885>.
- [101] L. Truong-Phuoc, C. Duong-Viet, G. Tuci, A. Rossin, J.M. Nhut, W. Baaziz, O. Ersen, M. Arab, A. Jourdan, G. Giambastiani, C. Pham-Huu, Graphite Felt-Sandwiched Ni/SiC Catalysts for the Induction Versus Joule-Heated Sabatier Reaction: Assessing the Catalyst Temperature at the Nanoscale, *ACS Sustain. Chem. Eng.* 10 (2022) 622–632, <https://doi.org/10.1021/acssuschemeng.1c07217>.
- [102] L. Truong-Phuoc, C. Duong-Viet, G. Tuci, S. Sall, C. Petit, C. Sutter, M. Arab, A. Jourdan, C. Pham-Huu, Depleted uranium oxide supported nickel catalyst for autothermal CO<sub>2</sub> methanation in non-adiabatic reactor under induction heating, *Journal of Energy, Chemistry* 85 (2023) 310–323, <https://doi.org/10.1016/j.jechem.2023.06.035>.
- [103] M.G. Vinum, M.R. Almind, J.S. Engbæk, S.B. Vendelbo, M.F. Hansen, C. Frandsen, J. Bendix, P.M. Mortensen, Dual-Function Cobalt–Nickel Nanoparticles Tailored for High-Temperature Induction-Heated Steam Methane Reforming, *Angewandte Chemie - International Edition* 57 (2018) 10569–10573, <https://doi.org/10.1002/anie.201804832>.
- [104] M.R. Almind, S.B. Vendelbo, M.F. Hansen, M.G. Vinum, C. Frandsen, P. M. Mortensen, J.S. Engbæk, Improving performance of induction-heated steam methane reforming, *Catal. Today* 342 (2020) 13–20, <https://doi.org/10.1016/j.cattod.2019.05.005>.
- [105] M.R. Almind, M.G. Vinum, S.T. Wismann, M.F. Hansen, S.B. Vendelbo, J. S. Engbæk, P.M. Mortensen, I. Chorkendorff, C. Frandsen, Optimized CoNi Nanoparticle Composition for Curie-Temperature-Controlled Induction-Heated Catalysis, *ACS Appl. Nano Mater.* 4 (2021) 11537–11544, <https://doi.org/10.1021/acsnano.1c01941>.
- [106] V. Poletto Dotsenko, M. Bellusci, A. Masi, D. Pietrogiamomi, F. Varsano, Improving the performances of supported NiCo catalyst for reforming of methane powered by magnetic induction, *Catal. Today* 418 (2023), <https://doi.org/10.1016/j.cattod.2023.114049>.
- [107] P.M. Mortensen, J.S. Engbæk, S.B. Vendelbo, M.F. Hansen, M. Østberg, Direct Hysteresis Heating of Catalytically Active Ni-Co Nanoparticles as Steam Reforming Catalyst, *Ind. Eng. Chem. Res.* 56 (2017) 14006–14013, <https://doi.org/10.1021/acs.iecr.7b02331>.
- [108] A. Mohanty, C.D. Viet, A.C. Roger, A. Adam, D. Mertz, W. Baaziz, I. Janowska, Structural impact of carbon nanofibers/few-layer-graphene substrate decorated

- with Ni for CO<sub>2</sub> methanation via inductive heating, *Appl Catal B* 298 (2021), <https://doi.org/10.1016/j.apcatb.2021.120589>.
- [109] H.M. Nguyen, C.M. Phan, S. Liu, C. Pham-Huu, L. Nguyen-Dinh, Radio-frequency induction heating powered low-temperature catalytic CO<sub>2</sub> conversion via bi-reforming of methane, *Chem. Eng. J.* 430 (2022), <https://doi.org/10.1016/j.cej.2021.132934>.
- [110] C. Scarfiello, M. Bellusci, L. Pilloni, D. Pietrogiacomi, A. La Barbera, F. Varsano, Supported catalysts for induction-heated steam reforming of methane, *Int. J. Hydrogen Energy* 46 (2021) 134–145, <https://doi.org/10.1016/j.ijhydene.2020.09.262>.
- [111] F. Varsano, M. Bellusci, A. La Barbera, M. Petrecca, M. Albino, C. Sangregorio, Dry reforming of methane powered by magnetic induction, *Int. J. Hydrogen Energy* 44 (2019) 21037–21044, <https://doi.org/10.1016/j.ijhydene.2019.02.055>.
- [112] F. Varsano, M. Bellusci, A. Provino, M. Petrecca, NiCo as catalyst for magnetically induced dry reforming of methane, in: IOP Conf Ser Mater Sci Eng, Institute of Physics Publishing, 2018. <https://doi.org/10.1088/1757-899X/323/1/012005>.
- [113] J. Huang, W. Zhou, X. Luo, Y. Ding, D. Peng, M. Chen, H. Zhou, C. Hu, C. Yuan, S. Wang, Enhancing hydrogen evolution reaction of confined monodispersed NiSe<sub>2</sub>–X nanoparticles by high-frequency alternating magnetic fields, *Chem. Eng. J.* 454 (2023), <https://doi.org/10.1016/j.cej.2022.140279>.
- [114] D. Lach, B. Tomiczek, T. Siudyga, M. Kapkowski, R. Sitko, J. Klimontko, S. Golba, G. Dercz, K. Matus, W. Borek, J. Polanski, Spatially Formed Tenacious Nickel-Supported Bimetallic Catalysts for CO<sub>2</sub> Methanation under Conventional and Induction Heating, *Int. J. Mol. Sci.* 24 (2023), <https://doi.org/10.3390/ijms24054729>.
- [115] J. Polanski, P. Bartczak, W. Ambroziewicz, R. Sitko, T. Siudyga, A. Mianowski, J. Szade, K. Balin, J. Lelątko, Ni-supported Pd nanoparticles with Ca promoter: A new catalyst for low-temperature ammonia cracking, *PLoS One* 10 (2015), <https://doi.org/10.1371/journal.pone.0136805>.
- [116] C. Cerezo-Navarrete, I.M. Marin, C. Marini, B. Chaudret, L.M. Martínez-Prieto, Structural transformation of carbon-encapsulated core-shell CoNi nanoparticles during magnetically induced CO<sub>2</sub> reduction into CO, *Appl Catal B* 347 (2024), <https://doi.org/10.1016/j.apcatb.2024.123780>.
- [117] Q. Liu, S. McNair, F. Nichols, B. Lu, B. Yu, D. Pan, J. Ko, A. Bhuller, F. Bridges, S. Chen, Ultrafast synthesis of cobalt/carbon nanocomposites by magnetic induction heating for oxygen evolution reaction, *Adv. Sens. Energy Mater.* 2 (2023) 100046, <https://doi.org/10.1016/j.asesm.2023.100046>.
- [118] G. Zhou, P. Wang, H. Li, B. Hu, Y. Sun, R. Huang, L. Liu, Spin-state reconfiguration induced by alternating magnetic field for efficient oxygen evolution reaction, *Nat. Commun.* 12 (2021), <https://doi.org/10.1038/s41467-021-25095-4>.
- [119] A. Crisbasan, D. Chaumont, M. Sacilotto, A. Crisan, A.M. Lazar, I. Ciobanu, Y. Lacroute, R. Chassagnon, Study of TiO<sub>2</sub> nanomembranes obtained by an induction heated MOCVD reactor, *Appl. Surf. Sci.* 358 (2015) 655–659, <https://doi.org/10.1016/j.apsusc.2015.09.113>.
- [120] X. Gong, Z. Jiang, W. Zeng, C. Hu, X. Luo, W. Lei, C. Yuan, Alternating Magnetic Field Induced Magnetic Heating in Ferromagnetic Cobalt Single-Atom Catalysts for Efficient Oxygen Evolution Reaction, *Nano Lett.* 22 (2022) 9411–9417, <https://doi.org/10.1021/acs.nanolett.2c03359>.
- [121] W. Zeng, Z. Jiang, X. Gong, C. Hu, X. Luo, W. Lei, C. Yuan, Atomic Magnetic Heating Effect Enhanced Hydrogen Evolution Reaction of Gd@MoS<sub>2</sub> Single-Atom Catalysts, *Small* 19 (2023), <https://doi.org/10.1002/smll.202206155>.
- [122] S. Chatterjee, V. Degirmenci, F. Aiouache, E.V. Rebrov, Design of a radio frequency heated isothermal micro-trickle bed reactor, *Chem. Eng. J.* 243 (2014) 225–233, <https://doi.org/10.1016/j.cej.2013.12.059>.
- [123] S. Chatterjee, T.K. Houlding, V.Y. Doluda, V.P. Molchanov, V.G. Matveeva, E. V. Rebrov, Thermal Behavior of a Catalytic Packed-Bed Milli-reactor Operated under Radio Frequency Heating, *Ind. Eng. Chem. Res.* 56 (2017) 13273–13280, <https://doi.org/10.1021/acs.iecr.7b01723>.
- [124] M. Osial, A. Pregorwska, The Application of Artificial Intelligence in Magnetic Hyperthermia Based Research, *Future Internet* 14 (2022), <https://doi.org/10.3390/fi14120356>.